



Estimation of the 3-D geoelectric field at the Earth's surface using Spherical Elementary Current Systems

Liisa Juusola¹, Heikki Vanhamäki², Elena Marshalko¹, Mikhail Kruglyakov³, and Ari Viljanen¹

¹Finnish Meteorological Institute, Helsinki, Finland

²University of Oulu, Oulu, Finland

³University of Otago, Dunedin, New Zealand

Correspondence: Liisa Juusola (liisa.juusola@fmi.fi)

Abstract. The geoelectric field drives geomagnetically induced currents (GIC) in technological conductor networks, which can affect the performance of critical ground infrastructure such as electric power transmission grids. The three-dimensional (3-D) electric field at the Earth's surface consists of an external divergence-free (DF) part due to temporally and spatially varying ionospheric and magnetospheric currents, an internal DF part due to temporally and spatially varying telluric currents, and a curl-free (CF) part due to charge accumulation at ground conductivity gradients. We have developed a new method for estimating these contributions. The external and internal parts of the DF electric field are calculated from the time derivative of the external and internal parts of the observed ground magnetic field, respectively, using DF two-dimensional (2-D) Spherical Elementary Current Systems (SECS). The horizontal surface CF electric field is calculated from the known surface DF electric field using coefficients that linearly relate the DF electric field to the CF electric field. The coefficients were obtained from the 3-D induction model PGIEM2G (Kruglyakov and Kuvshinov, 2018). The calculations are carried out in the time domain and only two consecutive time steps of the observed magnetic field are needed to compute the surface electric field. The external part of the DF electric field is valid at and below the ionosphere, the internal part at and above the Earth's surface, and the CF part at the Earth's surface. A dense magnetometer network is a requirement for reliable results. The external and internal parts of the DF electric field are generally oppositely directed and have comparable amplitudes, both on the ground and in the ionosphere, indicating that both contributions are significant for the total DF electric field. The largest peaks of total DF electric field tend to occur when either the external or internal contribution is temporarily suppressed. At a given location, a DF electric field with a given amplitude can result in a total surface electric field amplitude with an orders of magnitude difference depending on the direction of the DF electric field with respect to the locally dominant conductivity gradient structure. The electric field calculation is computationally light, facilitating operational implementation of a near-real time 3-D surface electric field monitoring and derivation of long electric field time series.

1 Introduction

The geoelectric field at the Earth's surface drives geomagnetically induced currents (GIC) in technological conductor networks, which can affect the performance of critical ground infrastructure such as electric power transmission grids (Pulkkinen et al., 2017). In order to avoid incidents caused by space weather, solid understanding of the possible amplitude range of the highly



25 variable and location-dependent electric field is needed. Because electric field measurements are scarce, the surface electric field is typically modelled using magnetic field measurements and knowledge of the conductivity of the Earth. For the same reason, validation of the modelling results is difficult, which means that it would be useful to have several alternative approaches that would allow inter-comparison of various modelling results.

As follows from the Maxwell equations, the electric field \mathbf{E} can be expressed as

$$30 \quad \mathbf{E} = -\frac{\partial \mathbf{A}}{\partial t} - \nabla \phi \quad (1)$$

where \mathbf{A} is the vector potential and ϕ is the scalar potential. It is possible to require that the vector potential is divergence-free:

$$\nabla \cdot \mathbf{A} = 0 \quad (2)$$

This is known as the Coulomb gauge condition (Jackson, 1998). It follows that the scalar potential can be expressed in terms
35 of the charge density ρ as:

$$\phi(\mathbf{r}, t) = \frac{1}{4\pi\epsilon_0} \int_V \frac{\rho(\mathbf{r}', t)}{|\mathbf{r} - \mathbf{r}'|} dV' \quad (3)$$

where ϵ_0 is the vacuum permittivity. Contrary to the often applied Lorenz gauge, the time t is not retarded, but the scalar potential is formally identical to the static case.

In the Coulomb gauge, the vector potential is given by the divergence-free (DF) part of the current density \mathbf{J} :

$$40 \quad \mathbf{A}(\mathbf{r}, t) = \frac{\mu_0}{4\pi} \int_V \frac{\mathbf{J}_{DF}(\mathbf{r}', t - |\mathbf{r} - \mathbf{r}'|/c)}{|\mathbf{r} - \mathbf{r}'|} dV' \quad (4)$$

where μ_0 is the vacuum permeability and c is the speed of light. Note that here the time is retarded.

The power of the Coulomb gauge is that it automatically separates the electric field into a curl-free (CF) static part and a divergence-free inductive part:

$$\mathbf{E} = \mathbf{E}_{CF} + \mathbf{E}_{DF} \quad (5)$$

45 where

$$\mathbf{E}_{CF} = -\nabla \phi, \quad \mathbf{E}_{DF} = -\frac{\partial \mathbf{A}}{\partial t} \quad (6)$$

and \mathbf{E}_{CF} is produced only by charges and \mathbf{E}_{DF} only by divergence-free currents as explicitly shown above.

The DF electric field is directly associated with temporal variations of the magnetic field via Faraday's law, and can be further separated into an external part due to time-varying ionospheric and magnetospheric currents in space and into an internal part
50 due to telluric currents in the conducting Earth. The CF part is created by electric charges accumulated at conductivity gradients in the ground. There can also be charges in the ionosphere and upper space. However, they are quasi-static and the related electric field is confined between the ionosphere and Earth's surface and is perpendicular to the surface.



Several modelling techniques for estimating the surface electric field exist, either based on one-dimensional (1-D) ground conductivity models (Viljanen et al., 2004, 2012, 2014), magnetotelluric transfer functions (Kelbert et al., 2017; Love et al., 2018; Lucas et al., 2020; Malone-Leigh et al., 2023), or three-dimensional (3-D) ground conductivity models (Kruglyakov and Bloshanskaya, 2017; Rosenqvist and Hall, 2019; Marshalko et al., 2021; Kruglyakov et al., 2022; Marshalko et al., 2023; Kruglyakov et al., 2023). 1-D modelling only considers vertical conductivity gradients, and consequently ignores lateral gradients, which are now known to be highly significant (Marshalko et al., 2021). The magnetotelluric transfer functions take lateral conductivity gradients into account but ignore spatial variations in the source, which are also known to be important (Lucas et al., 2018; Marshalko et al., 2021). 3-D electromagnetic modelling considers both vertical and lateral conductivity gradients and can also take into account spatial variations of the inducing source, but as a result of sparse magnetometer coverage and inaccuracies in 3-D conductivity models, the internal part of the magnetic field variations is not conserved (Kruglyakov et al., 2023; Marshalko et al., 2023). They can also be computationally expensive.

Vanhamäki et al. (2013) developed a method for calculating the DF surface electric field using the two-dimensional (2-D) Spherical Elementary Current System (SECS) method (Amm, 1997; Amm and Viljanen, 1999; Pulkkinen et al., 2003a, b; McLay and Beggan, 2010; Weygand et al., 2011; Juusola et al., 2016; Marsal et al., 2017, 2020; Juusola et al., 2020; Laundal et al., 2021; Vanhamäki and Juusola, 2020; Walker et al., 2023). Their approach was to place a DF 2-D SECS layer in the ionosphere at 100 km altitude, to determine the SECS amplitudes by fitting the superposed vertical magnetic field components (B_r) of the SECSs to the measured vertical magnetic field components on the ground, to derive the horizontal component of the vector potential (A_h) by applying the equation for the vector potential of the DF 2-D SECS from Amm and Viljanen (1999), and to calculate the DF electric field from the time derivative of the vector potential as

$$\mathbf{E}_{DF,h} = -\frac{\partial \mathbf{A}_h}{\partial t}. \quad (7)$$

They also discussed the possibility of deriving the CF part of the surface electric field from the known ground surface conductivity and the requirement that the total current is divergence-free.

We will continue the work by Vanhamäki et al. (2013) by deriving a method for calculating the internal and external part of the DF electric field at and above the Earth's surface and the CF electric field at the Earth's surface. Similar to Vanhamäki et al. (2013), we will utilize the DF 2-D SECSs to calculate the DF electric field, but in addition to the ionospheric DF SECS layer, we will place a second layer just below the Earth's surface. This allows us to fit all three components of the measured magnetic field when determining the SECS amplitudes, to derive a solution that is valid not only at the Earth's surface but above it as well, and to separate the internal and external part of the DF electric field. We will implement and test the calculation for the CF electric field suggested by Vanhamäki et al. (2013). However, we will show that the required assumption of vanishing radial currents is too restrictive and instead derive coefficients based on the 3-D induction model PGIEM2G (Polynomial Galerkin Integral Equation Modelling in ElectroMagnetic Geophysics) (Kruglyakov and Bloshanskaya, 2017; Kruglyakov and Kuvshinov, 2018) that linearly relate the DF electric field to the horizontal CF electric field at the Earth's surface. PGIEM2G is a scalable 3-D electromagnetic forward modelling code based on a method of volume integral equations with a contracting kernel (Kruglyakov and Kuvshinov, 2018).



3-D induction modelling codes such as PGIEM2G determine total electric and magnetic fields by solving Maxwell's equations numerically for a given 3-D conductivity model and given inducing source. Such an approach requires relatively long time integration, during which inaccuracies can accumulate, and is sensitive to the available conductivity model. Our approach has the advantage that in addition to the external part of the DF electric field, the internal part of the DF electric field is also derived from measurement. Thus, no conductivity model is needed to determine the DF part of the electric field (information on the conductivity is automatically included in the measured magnetic field) and no time integration is required. However, the sensitivity to the magnetometer coverage remains, as does the dependence of the CF part of the electric field on the conductivity model.

Although 3-D induction modelling codes are very rigorous and can model ground induction as far as limited magnetic field observations and 3-D ground conductivity models allow, this does not mean induction is perfectly understood. The geoelectric field is deterministic but highly unpredictable. In other words, the electric field can be precisely calculated from a given external source and a known ground conductivity. In practice, it is difficult to give any simple rules of how the ground responds to a large variety of different external drivers such as sudden impulses, temporally varying large-scale electrojets, current vortices, etc. As Juusola et al. (2020) show, the internal part of the time derivative of the horizontal ground magnetic field ($d\mathbf{H}/dt$) has a much more complex spatial structure than the relatively smooth external $d\mathbf{H}/dt$. The contrast becomes even more pronounced when comparing the external driver and the geoelectric field (Marshalko et al., 2023). Separation of the various components of the surface electric field (external and internal parts of the DF electric field and the CF electric field) provides a tool for deepening our understanding, including the combination of external driving and ground conductivity structures that pose the most severe risks for technological conductor networks. Such understanding is particularly useful for space weather services and power grid operators. Furthermore, computationally reasonable methods allow the production of long time series of surface electric field data, which can be used as material for extreme value analysis to better understand the threats of severe space weather events.

The structure of the study is as follows: the method is derived in Section 2, test results are presented and validated in Section 3, and further applications are discussed in Section 4. The conclusions are summarised in Section 5.

2 Theory

In this section, we will first derive the method for obtaining the external and internal parts of the DF electric field at and above the Earth's surface from ground magnetic field measurements using DF 2-D SECSs (Section 2.1). In Section 2.2 we will derive the method for estimating the CF surface electric field from a known DF electric field, surface conductance, and vertical current density.

2.1 DF electric field of a DF 2-D SECS with a time-varying amplitude

The DF part of the electric field (\mathbf{E}) due to a time-varying magnetic field (\mathbf{B}) can be solved from Faraday's law,

$$\nabla \times \mathbf{E}_{DF} = -\frac{\partial \mathbf{B}}{\partial t}. \quad (8)$$



DF 2-D SECSs form a complete set of basis functions for representing ground magnetic field variations in terms of external
 120 and internal equivalent currents (Vanhamäki and Juusola, 2020). The time-varying sheet current density of the DF 2-D SECS
 (Amm, 1997) is

$$\mathbf{J}_{DF}(t) = \frac{I_{DF}(t)}{4\pi R} \cot\left(\frac{\theta'}{2}\right) \hat{\mathbf{e}}_{\phi'}, \quad (9)$$

where $I_{DF}(t)$ is the time-varying amplitude in A, R is the radius of the current sheet, and θ' is the colatitude in the SECS
 coordinates. Conversion to general coordinates, e.g., geographic, follows the regular practise of the 2-D SECS method (Van-
 125 hamäki and Juusola, 2020). In the SECS coordinates, the time derivative of the DF 2-D SECS magnetic field only has r and θ'
 components (Amm and Viljanen, 1999),

$$\frac{\partial \mathbf{B}}{\partial t} = \frac{\partial B_r}{\partial t} \hat{\mathbf{e}}_r + \frac{\partial B_{\theta'}}{\partial t} \hat{\mathbf{e}}_{\theta'}, \quad (10)$$

where

$$\frac{\partial B_r}{\partial t} = \frac{\partial I_{DF}}{\partial t} \frac{\mu_0}{4\pi r} \left(\frac{R}{\sqrt{r^2 - 2rR\cos\theta' + R^2}} + \begin{cases} -1 & \text{when } r < R \\ -R/r & \text{when } r \geq R \end{cases} \right) \quad (11)$$

130 and

$$\frac{\partial B_{\theta'}}{\partial t} = -\frac{\partial I_{DF}}{\partial t} \frac{\mu_0}{4\pi r \sin\theta'} \left(\frac{r - R\cos\theta'}{\sqrt{r^2 - 2rR\cos\theta' + R^2}} + \begin{cases} \cos\theta' & \text{when } r < R \\ -1 & \text{when } r > R \end{cases} \right) \quad (12)$$

Consequently, the induced electric field only has a ϕ' component,

$$\mathbf{E}_{DF} = E_{DF,\phi'} \hat{\mathbf{e}}_{\phi'}, \quad (13)$$

which can be solved from the integral form of Equation 8,

$$135 \oint_{\partial A} \mathbf{E}_{DF} \cdot d\mathbf{l} = -\frac{\partial}{\partial t} \int_A \mathbf{B} \cdot d\mathbf{S} \quad (14)$$

by calculating the change in the magnetic flux through the spherical cap surface defined by a field line of $E_{DF,\phi'}$ (Figure 1),

$$2\pi r \sin\theta' E_{DF,\phi'} = -r^2 \int_0^{\theta'} d\theta \sin\theta \int_0^{2\pi} d\phi \frac{\partial B_r}{\partial t}. \quad (15)$$

Carrying out the calculation yields

$$E_{DF,\phi'} = -\frac{\partial I_{DF}}{\partial t} \frac{\mu_0}{4\pi r \sin\theta'} \left(\sqrt{r^2 - 2rR\cos\theta' + R^2} + \begin{cases} r\cos\theta' - R & \text{when } r < R \\ R\cos\theta' - r & \text{when } r \geq R \end{cases} \right) \quad (16)$$

140 which is equal to the negative time derivative of the vector potential (Eq. 7) given by Amm and Viljanen (1999) for the DF
 SECS when $r < R$. Comparison of Eq. 16 with Eq. 9 confirms that the induced electric field opposes the temporal change of
 the DF current, as expected from Lenz's law.

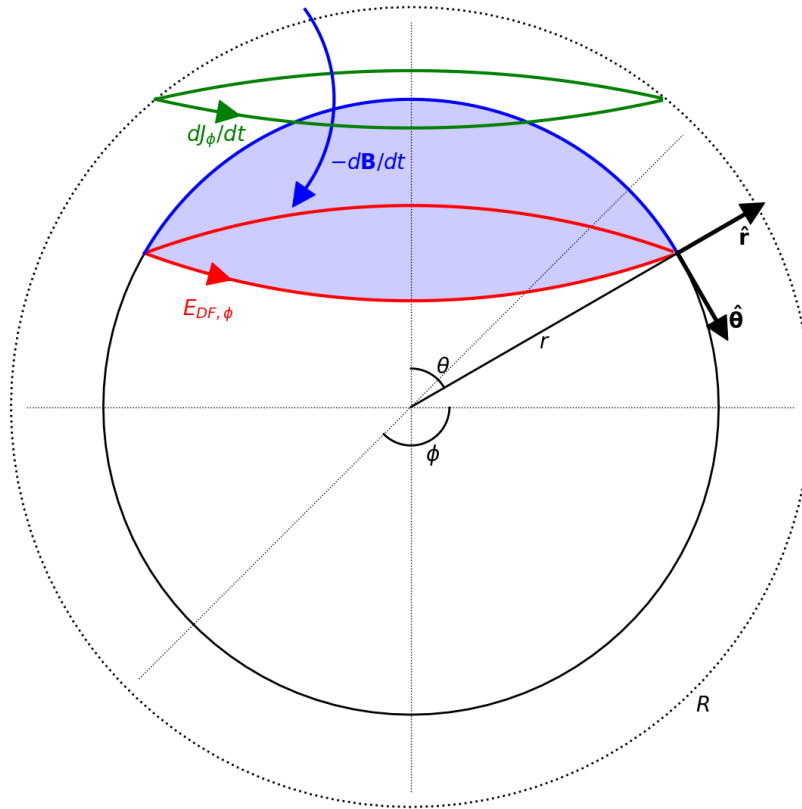


Figure 1. Geometry of the derivation of the divergence-free (DF) electric field ($E_{DF,\phi}$) of a DF 2-D Spherical Elementary Current System (SECS) with a time-varying amplitude. J_ϕ indicates the SECS current density, B its magnetic field, and d/dt the time derivative. r , θ , and ϕ are spherical coordinates (radius, co-latitude, and longitude) and \hat{r} , $\hat{\theta}$, $\hat{\phi}$ the corresponding unit vectors.

Figure 2 shows co-latitude profiles of $\partial J_\phi/\partial t$, ground $\partial B_r/\partial t$, ground $\partial B_\theta/\partial t$, and ground $E_{DF,\phi}$ for two different cases: J_ϕ at 90 km altitude (blue curves, external contribution) and oppositely directed J_ϕ at 2×90 km depth (red curves, internal contribution), to mimic a simple case of ionospheric and telluric currents. Both have the same amplitude $|\partial I_{DF}/\partial t| = 10$ kA/s. The sum of the external and internal $\partial B_r/\partial t$, $\partial B_\theta/\partial t$, and E_ϕ on the ground are shown by the black curves. While the current density is concentrated near the SECS pole at $\theta = 0$, the magnetic field is more spread out to lower latitudes, and the DF electric field even more so. On the ground, the horizontal magnetic field components B_θ from the oppositely directed ionospheric and telluric currents strengthen each other, while the vertical components B_r tend to cancel each other out. The DF electric fields also tend to cancel each other out, resulting in a much weaker total ground DF electric field than either the original ionospheric or telluric contribution.



The time derivative of the SECS amplitude can be estimated from the known amplitudes I_{DF} as

$$\frac{\partial I_{DF}}{\partial t} = \frac{I_{DF}(t) - I_{DF}(t - \Delta t)}{\Delta t}, \quad (17)$$

where Δt is the time step of the data. When both the ionospheric equivalent current amplitudes at 90 km altitude and telluric
 155 equivalent current amplitudes at 1 m depth have been determined from ground magnetic field observations (Juusola et al.,
 2016, 2020; Vanhamäki and Juusola, 2020), Eq. 16 can be used to estimate the ionospheric DF current contribution to \mathbf{E}_{DF}
 everywhere and telluric current contribution to \mathbf{E}_{DF} at and above the Earth's surface.

2.2 CF electric field at the Earth's surface driven by the DF electric field

The DF electric field in the conducting Earth has an external and an internal component. The external component is produced
 160 by time-varying ionospheric and magnetospheric current systems, and the internal component by time-varying 3-D telluric
 currents. This electric field drives the electric currents in the Earth. Whenever the current driven by the DF electric field crosses
 a conductivity gradient, there is divergence of the current. Because the total current must be divergence-free (follows from
 neglecting the displacement current, as usual in geoelectromagnetism), a curl-free (CF) electric field is set up by redistribution
 of electric charges in the Earth to satisfy this condition. The divergence of the total current can be written as

$$165 \quad \nabla \cdot \mathbf{j} = \nabla \cdot (\sigma \mathbf{E}_{DF} + \sigma \mathbf{E}_{CF}) = \nabla \sigma \cdot \mathbf{E}_{DF} + \sigma \nabla \cdot \mathbf{E}_{DF} + \nabla \sigma \cdot \mathbf{E}_{CF} + \sigma \nabla \cdot \mathbf{E}_{CF}, \quad (18)$$

where σ is the known electrical conductivity. The DF electric field is a superposition of the external and internal contribution
 and satisfies

$$\nabla \cdot \mathbf{E}_{DF} = 0. \quad (19)$$

We will only consider the surface layer of the conducting Earth and model it as an infinitely thin conducting sheet located at
 170 the Earth's surface. Equation 18 then becomes

$$\nabla \Sigma \cdot \mathbf{E}_{CF} + \Sigma \nabla \cdot \mathbf{E}_{CF} = -\nabla \Sigma \cdot \mathbf{E}_{DF} + j_r, \quad (20)$$

where Σ is the conductance of the thin sheet, obtained by vertical integration of the conductivity in the surface layer, and j_r is
 the vertical current density.

We use CF SECS functions to solve \mathbf{E}_{CF} when Σ and \mathbf{E}_{DF} are known. The electric field of a CF SECS is

$$175 \quad \mathbf{E}_{CF} = \frac{Q_{CF}}{4\pi R} \hat{\mathbf{e}}_{\theta'} \begin{cases} \cot\left(\frac{\theta'}{2}\right) & \text{when } \theta' \geq \theta_0 \\ \tan\left(\frac{\theta'}{2}\right) \cot^2\left(\frac{\theta_0}{2}\right) & \text{when } \theta' < \theta_0 \end{cases}, \quad (21)$$

where the electric charge Q_{CF} determines the amplitude of the CF SECS, R is the radius of the surface, and θ' is the colatitude
 in the SECS coordinates. The source at the elementary current system's pole is spread uniformly inside a spherical cap of width
 θ_0 . The divergence of \mathbf{E}_{CF} is given by

$$\nabla \cdot \mathbf{E}_{CF} = \frac{\rho}{\epsilon_0} = -\frac{Q_{CF}}{4\pi R^2 \epsilon_0} + \begin{cases} 0 & \text{when } \theta' \geq \theta_0 \\ \frac{Q_{CF}}{A \epsilon_0} & \text{when } \theta' < \theta_0 \end{cases}, \quad (22)$$



180 where ρ is the charge density and A is the area of the spherical cap defined by θ_0 ,

$$A = 2\pi R^2(1 - \cos \theta_0). \quad (23)$$

The total CF electric field in the grid cell i is a superposition of the electric fields of all the CF SECSs. Eq. 20 can now be written as

$$\sum_j \left[\nabla \Sigma_{\theta,i} g_{\theta,i,j} + \nabla \Sigma_{\phi,i} g_{\phi,i,j} - \Sigma_i \frac{1}{4\pi R^2} \right] \frac{Q_{CF,j}}{\epsilon_0} + \Sigma_i \frac{Q_{CF,i}}{A_i \epsilon_0} = -\nabla \Sigma_{\theta,i} E_{DF\theta,i} - \nabla \Sigma_{\phi,i} E_{DF\phi,i} + j_{r,i}, \quad (24)$$

185 where we have denoted the geometry-dependent components of \mathbf{E}_{CF} by g . By assuming that the radial current either vanishes ($j_{r,i} = 0$) or is otherwise known, the amplitudes $Q_{CF,i}$ can be determined from the matrix equation corresponding to Eq. 24. No time-integration of currents is needed, because the internal contribution to \mathbf{E}_{DF} is obtained from measurements. Thus, only two time steps of data are needed to determine the geoelectric field at the Earth's surface for a given epoch.

3 Test examples

190 Marshalko et al. (2021) have used PGIEM2G to model the 3-D geoelectric field during the September 7–8 2017 storm. They show the resulting horizontal geoelectric field for two epochs, 23:16 UT and 23:52 UT. We use these epochs to test our method. Marshalko et al. (2021) ran their simulation using inducing source data with 1 min temporal resolution as an input, but we compare our results with a rerun that used 10 s data.

3.1 DF electric field

195 We have used 10 s ground magnetic field measurements from the International Monitor for Auroral Geomagnetic Effects (IMAGE) magnetometers (Juusola et al., 2024). After correcting the data for any erroneous spikes and jumps, a 10-day sliding median baseline was subtracted from the data. DF 2-D SECS poles were placed in the IMAGE region on uniform grids with 0.5° latitude and 1° longitude resolution at 1 m depth and at 90 km altitude, and their amplitudes were determined by fitting the superposed magnetic field of the SECSs to the three components of the measured magnetic field (Vanhamäki and Juusola, 200 2020). The time derivative of the SECS amplitudes was derived using Eq. 17 and the DF electric field using Eq. 16 combined with the regular coordinate manipulations of the SECS method (Vanhamäki and Juusola, 2020). Because in this application of the 2-D SECS method we are only interested in $\partial \mathbf{B} / \partial t$ and not \mathbf{B} , it would also be possible to skip the baseline subtraction and directly fit $\partial \mathbf{B} / \partial t$ with the DF 2-D SECS functions.

Figure 3 shows the resulting external, internal, and total time derivative of the ground magnetic field ($\partial \mathbf{B} / \partial t$) and the DF 205 electric field (\mathbf{E}_{DF}) and its curl (Eq. 8) on 7 Sep 2017 at 23:16 UT. \mathbf{E}_{DF} is smoother than $\partial \mathbf{B} / \partial t$ but peaks in the same general area as the horizontal part of $\partial \mathbf{B} / \partial t$, as expected. Fig. 3 also demonstrates that the internal parts have much more pronounced spatial variability than the relatively smoothly varying external parts. External sources are located more than ~ 100 km from the ground points, whereas internal sources (telluric currents) are concentrated close to the surface and strongly modulated by conductivity gradients. The direction of the internal part of \mathbf{E}_{DF} is opposite to that of the external part of \mathbf{E}_{DF} , and has a



210 slightly weaker amplitude. As a result, the total \mathbf{E}_{DF} has a clearly weaker amplitude and different distribution than the external
 and internal parts. Similar plots for the epoch 23:52 UT are shown in Figure 4. The overall amplitude level of the DF electric
 field of hundreds of mV/km is in agreement with the theoretical examples of Vanhamäki et al. (2013). The curl $(\nabla \times \mathbf{E})_r$
 equals $-\partial B_r / \partial t$ and $\partial \mathbf{B} / \partial t$ is conserved. It should be noted that this does not guarantee that the separation into internal and
 external parts is entirely correct. The two sources may get mixed to some degree, especially in areas where the magnetometer
 215 coverage is sparse (Juusola et al., 2020).

3.2 CF electric field

Similar to Marshalko et al. (2021), we have used the SMAP model (Korja et al., 2002) to estimate the ground conductivity σ .
 SMAP provides the conductivity with a 5' latitude and 5' longitude resolution. The conductivity distribution in the top 0–10 km
 layer is displayed in Figure 5.

220 We have determined the CF SECS amplitudes on a grid where the conductance, its gradient, and grid cell area are obtained
 with the finite difference approach

$$\Sigma_{i,j} = \sigma_{i,j} \cdot 10 \text{ km} \quad (25)$$

$$\Sigma_{i+\frac{1}{2},j+\frac{1}{2}} = \frac{\Sigma_{i,j} + \Sigma_{i+1,j} + \Sigma_{i,j+1} + \Sigma_{i+1,j+1}}{4} \quad (26)$$

$$\nabla \Sigma_{\theta, i+\frac{1}{2}, j+\frac{1}{2}} = \frac{1}{2} \cdot \left(\frac{\Sigma_{i+1,j} - \Sigma_{i,j}}{R_E \Delta \theta} + \frac{\Sigma_{i+1,j+1} - \Sigma_{i,j+1}}{R_E \Delta \theta} \right) \quad (27)$$

$$225 \nabla \Sigma_{\phi, i+\frac{1}{2}, j+\frac{1}{2}} = \frac{1}{2} \cdot \left(\frac{\Sigma_{i,j+1} - \Sigma_{i,j}}{R_E \sin \theta_{\phi, i+\frac{1}{2}, j+\frac{1}{2}} \Delta \phi} + \frac{\Sigma_{i+1,j+1} - \Sigma_{i+1,j}}{R_E \sin \theta_{\phi, i+\frac{1}{2}, j+\frac{1}{2}} \Delta \phi} \right) \quad (28)$$

$$A_{i+\frac{1}{2}, j+\frac{1}{2}} = 2R_E^2 \Delta \phi \sin \theta_{i+\frac{1}{2}, j+\frac{1}{2}} \sin \frac{\Delta \theta}{2} \quad (29)$$

$$j_{r, i+\frac{1}{2}, j+\frac{1}{2}} = 0. \quad (30)$$

Here, R_E is the Earth radius, $\Delta \theta$ and $\Delta \phi$ are the colatitude and longitude resolution of the original conductivity grid, i is an
 index of the colatitude grid and j an index of the longitude grid. As we do not have any information of the vertical current
 density, it is assumed to vanish. The SECS polar cap angle θ_0 was calculated from the grid cell area using Eq. 23. The final CF
 230 electric field was evaluated at the original conductance grid, i.e., at grid points (i, j) .

Because of the computational limitations of a regular laptop, some optimization of the CF electric field calculation was
 needed to process the full IMAGE area: We split the conductivity model area into 240 pieces with an extent of 2° in latitude
 with $\pm 2^\circ$ padding and 1.9° in longitude with $\pm 4^\circ$ padding. The full area was assembled by fitting these 240 subareas together.
 235 This approximation did not extend to the DF electric field calculation, for which the full area was utilized. Naturally, the best
 approach would be to utilize more powerful computing resources, so that no optimization would be needed at all. For our
 simple test the approximation suffices.

Figure 6 displays the resulting charge density (left column), amplitude of the horizontal part of the CF electric field \mathbf{E}_{CF}
 (middle column), and total electric field $\mathbf{E}_{DF} + \mathbf{E}_{CF}$ (right column) for the two epochs in Fig. 3 (top row) and Fig. 4 (bottom
 240 row). The edges of the computational subareas can be detected in some regions, indicating that larger areas would be better.



As expected, charges accumulate at conductivity gradients, resulting in a total electric field that is generally higher in areas of lower conductivity and lower in areas of higher conductivity.

3.3 Comparison with PGIEM2G

In this section, we compare the electric field modelled using the SECS-method with the electric field modelled using PGIEM2G (Kruglyakov and Bloshanskaya, 2017; Kruglyakov and Kuvshinov, 2018). Calculations in PGIEM2G code are carried out in Cartesian geometry for planar Earth. To make a transition from spherical to Cartesian geometry, a map projection (Transverse Mercator in the case of Fennoscandia) and interpolation onto a regular grid (about 5×5 km) is first performed for the SMAP (and inducing source) data. Then an inverse transformation and interpolation onto a regular grid is carried out for resulting electric and magnetic fields to obtain data in spherical geometry. The final spatial resolution of electric (and magnetic) fields is $0.03^\circ \times 0.07^\circ$ (in latitudinal and longitudinal directions, correspondingly). The discrepancy between the original model grid used in our calculations and the denser grid used in PGIEM2G is not considered an issue in our qualitative comparison. In the one case when we wish to insert part of the SMAP data directly into our model, nearest-neighbour interpolation is performed. The external source used in the PGIEM2G simulation is obtained using the SECS method.

The top left panel of Figure 7 shows the amplitude of the horizontal surface electric field modelled using PGIEM2G for the same epoch as the top right panel of Fig. 6. The rest of the panels show the DF part of the electric field and its curl (top right), CF part of the electric field (middle left), divergence of the electric field (middle right), and divergence of the horizontal current density divided by conductance (bottom left). We will come back to the bottom right panel later. Similar plots for the epoch shown in the bottom right panel of Fig. 6 can be found in Figure 8.

The DF part of the electric field was obtained using the modelled curl $(\nabla \times \mathbf{E})_r = -\frac{\partial B_r}{\partial t}$ to estimate DF SECS amplitudes I_{DF}

$$(\nabla \times \mathbf{E})_{r,i} = \frac{I_{DF,i}}{A_i} - \sum_j \frac{I_{DF,j}}{4\pi R^2} \quad (31)$$

$$I_{DF,i+\frac{1}{2},j+\frac{1}{2}} \approx A_{i+\frac{1}{2},j+\frac{1}{2}} (\nabla \times \mathbf{E})_{r,i+\frac{1}{2},j+\frac{1}{2}}. \quad (32)$$

The CF part of the electric field was obtained by subtracting the DF part of the electric field from the total electric field. The divergence of the electric field $(\nabla \cdot \mathbf{E})$ was estimated using finite difference calculation.

Comparison of the PGIEM2G and SECS results reveals that, unlike PGIEM2G, the SECS method does not produce a narrow band of intense CF electric field on the side of the low conductance at conductance gradients but enhances the electric field across the entire area of lower conductance. The SECS method assumes that vertical current density is zero, but clearly this is not a valid assumption, as can be seen by examining the divergence of the horizontal current density in the bottom left panel of Fig. 7 and Fig. 8. Comparison of these panels with the divergence of the electric field in the middle right panels confirms that vertical currents are clearly responsible for producing the second layer of charges near conductivity gradients that largely confine the CF electric field near the gradients.

Another possible source of discrepancy between PGIEM2G and the SECS method is the internal part of the DF electric field. Whereas the SECS method reconstructs it from measurements, PGIEM2G models it based on the 3-D conductivity of SMAP.



While sparse magnetometer coverage affects the DF electric field of the SECS method, inaccuracies in the conductivity model
275 affect PGIEM2G. The difference can be seen by comparing the respective DF electric fields in the bottom right panel of Fig. 3
and top right panel of Fig. 7 or the bottom right panel of Fig. 4 and top right panel of Fig. 8. PGIEM2G produces small-scale
structures that cannot be resolved with the operational magnetometers. On the other hand, the curl of the electric field from the
SECS method corresponds to the measured $-\partial B_r/\partial t$ at all IMAGE stations whereas for PGIEM2G this is not true, as can be
seen by comparing with $\partial B_r/\partial t$ in the top right panel of Fig. 3 and Fig. 4.

280 We test the above conclusions by running the SECS CF electric field calculation with PGIEM2GS DF electric field and
vertical current density. The resulting divergence of the electric field for the two epochs are given in the bottom right panels of
Fig. 7 and Fig. 8. Now there is much better correspondence between the SECS result and PGIEM2G result in the middle right
panel. Thus, we conclude that without knowledge of the vertical current density, the SECS method cannot reliably estimate the
CF part of the electric field. The DF part of the electric field, however, can be considered reliable, at least in areas where the
285 magnetometer coverage is good.

3.4 Coefficients relating E_{CF} to E_{DF}

As we cannot use the SECS method to estimate the CF part of the electric field, we try an alternative approach: We assume that
the CF electric field is approximately proportional to the driving DF electric field

$$E_{CF,x} = k_{xx}E_{DF,x} + k_{xy}E_{DF,y} \quad (33)$$

290 $E_{CF,y} = k_{yy}E_{DF,y} + k_{yx}E_{DF,x}.$ (34)

This formulation resembles that of magnetotelluric transfer functions, which define the frequency dependent linear relationship
(impedance tensors) between components of the electric field and horizontal components of the magnetic field variations
measured at a given location. Our formulation does not depend on frequency but is given in the time domain. This is possible,
because the internal part of the DF electric field is obtained from measurements and we only need a linear relationship for
295 describing the CF part of the electric field from the known DF part. The assumed linear relation contains a local plane wave
assumption, i.e., we assume that the spatial structures of the DF electric field are larger than the range of the relevant charge
accumulations that contribute to the local CF field. A more general relationship would be of the form $(E_{CF} \text{ values}) = \text{matrix} \cdot$
 $(E_{DF} \text{ values})$, with all grid points collected in the matrices. However, the simple plane wave assumption (i.e., the coefficient
matrix is diagonal) appears to be sufficient, as we will demonstrate below. In principle, it should be enough to determine
300 the time-independent coefficients from a single active interval. The most obvious problem would arise from a case where a
persistent small-scale DF electric field structure would bias the coefficients at some locations. However, the chaotic nature of
the time derivative of the magnetic field (Kellinsalmi et al., 2022) makes such a case unlikely, as long as the event chosen is
sufficiently long and active. Figure 9 shows the coefficients derived using the CF and DF part of PGIEM2G's horizontal surface
electric field between 7 September 2017 23:00 UT and 8 September 2017 01:00 UT. The standard deviation (STD) errors of
305 the coefficients are displayed in Figure 10. These are small compared to the values of the coefficients.



In order to examine the validity of Eq. 33–34, Figure 11 shows a time series of the CF electric field at SOD between 7 September 2017 23:00 UT and 8 September 2017 01:00 UT. The original modelled value is shown in black and the approximation based on Eq. 33–34 is shown in red. There is good correspondence between the original curve and approximation. Furthermore, the top row of Figure 12 shows maps of the CF part of the horizontal electric field modelled by PGIEM2G on 7 Sep 2017 at 23:16:00 UT (left) and at 23:52:00 UT (right), the CF electric field approximated using Eq. 33–34 with the coefficients from Fig. 9 and DF electric field from PGIEM2G (middle row), and the difference between the original and approximated CF field (bottom row). The differences are generally not very large, indicating that this approximation could be used to estimate the CF electric field from a known DF electric field.

In order to test the CF field approximation with IMAGE data, maps of the CF electric field approximated using Eq. 33–34 with the coefficients from Fig. 9 and DF electric field from SECS on 7 Sep 2017 at 23:16:00 UT (left) and at 23:52:00 UT (right) are shown in the top row of Figure 13. The bottom row shows the total electric field. Now the SECS method also produces similar electric field structures as PGIEM2G but there are some differences due to the DF electric field when comparing the CF electric field in Fig. 13 and Fig 12. Furthermore, Figure 14 shows E_x and E_y at SOD between 7 September 2017 23:00 UT and 8 September 2017 01:00 UT. PGIEM2G modelling is shown in black, SECS modelling based on IMAGE magnetic field in red, and SECS modelling based on PGIEM2G magnetic field in green. In addition, we have added estimates obtained via the multi-site transfer function (MSTF) (Kruglyakov et al., 2023) approach (blue curves). The MSTF approach is based on the use of transfer functions that relate the horizontal geoelectric field at any location in the modelling region with the horizontal magnetic field at (fixed) multiple locations. Note that MSTFs were calculated on the basis of the simulated electromagnetic fields (see Kruglyakov et al., 2023, for details). In Fig. 14, the SECS modelling based on IMAGE data shows peaks of higher amplitude than either PGIEM2G or the MSTF approach. Because the SECS modelling based on PGIEM2G magnetic field data has a much better agreement with PGIEM2G, the peaks in the IMAGE-based SECS are clearly due to the difference in the internal DF electric field.

Finally, Figure 15 shows a time series of the electric field as a sum of the external DF, internal DF, and CF parts, modelled using SECS at the location of the magnetometer station SOD between 7 September 2017 23:00 UT and 8 September 2017 01:00 UT. As can be seen from Fig. 5, SOD is located close to a conductivity gradient. The two top panels of Fig. 15 show the north (x) component of the electric field, the two middle panels show the east (y) component, and the two bottom panels show the amplitude. The external, internal, and total DF electric field are shown in the top, third, and fifth panel, and the total DF, CF, and total electric field in the second, fourth, and sixth panel. Comparison of the external, internal, and total DF electric field curves reveals that the total DF electric field is sometimes dominated by the external part, sometimes by the internal part, and sometimes large, oppositely directed peaks in both parts cancel each other out, producing a small total DF electric field. Comparison of the DF and CF electric field curves show that in the x direction, the CF electric field is directed in the same way as the DF electric field and has a larger amplitude than the DF electric field, resulting in a total electric field x component, which is clearly stronger than the DF electric field amplitude. In the y direction, the CF electric field also has a stronger amplitude than the DF electric field but the CF and DF part are oppositely directed, resulting in a total electric field that is stronger and oppositely directed to the DF electric field.



3.5 Comparison with observations

3.5.1 GIC observations

Recordings of geomagnetically induced currents (GIC) in the Finnish natural gas pipeline were carried out close to the Mäntsälä (MAN) compressor station in southern Finland (60.6 N, 25.2 E) from Nov 1998 to October 2023. The measurements were based on the differential magnetometer method, utilizing two magnetometers: one right above the pipe and the other at the nearby IMAGE station NUR (60.50 N, 24.65 E) (Pulkkinen et al., 2001). The quality of the MAN magnetometer data is variable, but good data is available for the Halloween storm 29–31 October 2003. GIC at MAN can also be estimated from the horizontal geoelectric field using the empirical expression (Pulkkinen et al., 2001; Viljanen et al., 2006)

$$GIC(t) = -70 \text{ A km V}^{-1} E_x(t) + 88 \text{ A km V}^{-1} E_y(t), \quad (35)$$

which assumes spatially uniform field in the region of the pipeline. In 2003, the magnetometer network around MAN was very sparse and the conductivity model in this region is known to be inaccurate (Marshalko et al., 2023), making direct comparison with the modelled electric field less than ideal. However, the linear relation between the DF electric field and $\frac{\partial \mathbf{B}}{\partial t}$ on the one hand, and the linear relation between the CF and DF electric field on the other hand, implies that the geoelectric field at location \mathbf{r} can be estimated from the magnetic field observations at locations \mathbf{r}_k^{obs} as

$$\mathbf{E}(\mathbf{r}, t) = \sum_{k=1}^{N_{obs}} Q(\mathbf{r}, \mathbf{r}_k^{obs}) \frac{\partial}{\partial t} \mathbf{B}(\mathbf{r}_k^{obs}, t), \quad (36)$$

where $Q(\mathbf{r}, \mathbf{r}_k^{obs})$ are 2×3 time-independent matrices. The Q matrices can be determined using PGIEM2G data, and bypass the need for the SECS expansion. However, unlike the SECS expansion, the Q matrices are rigid in terms of station configuration and introduce dependence on the conductivity model to the DF electric field. Determining the matrices will be a topic for a separate study.

For MAN, the contribution from the nearby magnetometer station NUR is likely to be much larger than that from the other, much more distant, stations. Combined with the linear approximation of Eq. 35, this allows us to estimate the GIC at MAN based on NUR $\frac{\partial \mathbf{B}}{\partial t}$ alone:

$$GIC(t) = a_x \frac{\partial B_x}{\partial t} + a_y \frac{\partial B_y}{\partial t} + a_z \frac{\partial B_z}{\partial t}. \quad (37)$$

To test this approach, we have used the period from 29 Oct 2003 08:00:00 UT to 31 October 2003 23:59:50 UT to determine the coefficients. The resulting values are provided in Table 1. Observed and modelled GIC for the immediately preceding period from 29 Oct 2003 06:00:00 UT to 07:59:50 UT are shown in Figure 16, and show good agreement in terms of time development and amplitude. The correlation coefficient is $CC = 0.80$ and the coefficient of determination

$$R^2 = 1 - \frac{\sum_i (GIC_i^{obs} - GIC_i^{mod})^2}{\sum_i (GIC_i^{obs} - \text{mean}(GIC^{obs}))^2} \quad (38)$$

is $R^2 = 0.64$.



Table 1. Coefficients for the linear relation of Eq. 37 between MAN GIC (in A) and NUR $\frac{\partial B}{\partial t}$ (in nT/s) obtained as a fit to the observed GIC from 29 Oct 2003 08:00:00 UT to 31 October 2003 23:59:50 UT. For comparison, the bottom set of coefficients is determined as a fit to the longer period from 29 Oct 2003 00:00:00 UT to 31 October 2003 23:59:50 UT.

Coefficient	Value	STD error
a_x	-1.69	0.01
a_y	-2.73	0.02
a_z	-0.23	0.02
a_x	-1.70	0.01
a_y	-2.71	0.02
a_z	-0.21	0.02

370 3.5.2 Electric field observations

Electric field observations suitable for comparison with modelling results are rare. However, there is an interval on 11 September 2005 from 05:15:00 UT to 06:15:00 UT with observations (Smirnov et al., 2006) from two sites near the IMAGE station MEK that has been used by Kruglyakov et al. (2023). Kruglyakov et al. (2023) called these sites M02 (63.043740 N, 30.657030 E) and M05 (62.938890 N, 30.993910 E). Similar to MAN, M02 and M05 are located in a region where the mag-
 375 netometer coverage is far from ideal. Thus, we will again utilize Eq. 36 and approximate the electric field components by fits to $\frac{\partial B}{\partial t}$ from the nearby station MEK (62.77 N, 30.97 E)

$$E_x = q_{xx} \frac{\partial B_x}{\partial t} + q_{xy} \frac{\partial B_y}{\partial t} + q_{xz} \frac{\partial B_z}{\partial t} \quad (39)$$

$$E_y = q_{yx} \frac{\partial B_x}{\partial t} + q_{yy} \frac{\partial B_y}{\partial t} + q_{yz} \frac{\partial B_z}{\partial t}. \quad (40)$$

Because the electric field components provided by Kruglyakov and Marshalko (2023) are in geomagnetic coordinates and
 380 the magnetic field observation from IMAGE in geographic, the coefficients also include rotation of the coordinate system. Geoelectric field observations contain effects due to charge build-up at local small-scale conductivity structures (see, e.g., Kruglyakov et al., 2023). These effects are also included in the coefficients. The coefficients resulting from fitting the period from 05:15:00–05:29:50 UT are provided in Table 2 and the observed and modelled electric field components are shown in Fig. 17. The period used for fitting is shaded. There is good agreement between the observed electric field components and the
 385 fits to MEK $\frac{\partial B}{\partial t}$ observations. For the period not used in the fitting, i.e., 05:30:00–06:15:00 UT, the correlation coefficients are 0.91 for M02 E_x , 0.95 for M02 E_y , 0.95 for M05 E_x , and 0.94 for M05 E_y . The coefficients of determination are 0.84 for M02 E_x , 0.89 for M02 E_y , 0.88 for M05 E_x , and 0.86 for M05 E_y . The good agreement between observations and modelling results here and in Section 3.5.1 support the assumptions of linear dependence between the parameters.



Table 2. Coefficients for the linear relations of Eq. 39–40 between M02 and M05 geomagnetic north (E_x) and south (E_y) components of the geoelectric field (in mV/km) and MEK geographic $\frac{\partial B}{\partial t}$ (in nT/s) obtained as a fit to the observed geoelectric field on 11 September 2005 from 05:15:00 to 05:29:50 UT.

Coefficient	Value	STD error
M02 q_{xx}	-39.85	8.74
M02 q_{xy}	139.11	8.82
M02 q_{xz}	-89.54	15.13
M02 q_{yx}	-56.73	9.28
M02 q_{yy}	44.27	9.37
M02 q_{yz}	-128.25	16.07
M05 q_{xx}	31.64	6.59
M05 q_{xy}	-8.34	6.65
M05 q_{xz}	71.20	11.41
M05 q_{yx}	-128.24	17.67
M05 q_{yy}	125.37	17.83
M05 q_{yz}	-263.88	30.59

4 Discussion

390 4.1 Maximum amplitudes of the event

The top part of Table 3 provides the times, locations, and amplitudes of the maximum electric field contributions on the ground in the IMAGE area during a geomagnetic storm between 7 September 2017 23:00:00 UT and 8 September 2017 01:00:00 UT (Dimmock et al., 2019; Juusola et al., 2023). The DF part of the electric has been calculated using the SECS method with IMAGE magnetic field as input and the CF electric field has been estimated using Eq. 33–34. The maximum of the external
 395 DF electric field took place on 7 Sep 2017 at 23:59:50 UT near stations ABK and AND. At this time, the total DF electric field also had a maximum in the same area, but a slightly larger value had already occurred earlier, at 23:15:30 UT, near station KIR, due to a temporary suppression of the internal part of the DF electric field around that location (not shown). The largest internal DF electric field occurred near station DON on 8 September at 00:30:00 UT. The CF electric field maximum occurred at the same time as the maximum of the external DF field, on 7 Sep 2017 at 23:59:50 UT, at a location a little southeast of
 400 RVK. Due to the very large amplitude of the CF field, this was also the time and location of the total electric field maximum.

The middle rows of Table 3 provides the times, locations, and amplitudes of the maximum time derivative of the horizontal magnetic field

$$\left| \frac{\partial \mathbf{H}(t)}{\partial t} \right| = \frac{\sqrt{[B_x(t) - B_x(t - \Delta t)]^2 + [B_y(t) - B_y(t - \Delta t)]^2}}{\Delta t} \quad (41)$$



Table 3. Time, location, and amplitude of the maximum horizontal electric field contributions and time derivative of the horizontal magnetic field ($|\partial\mathbf{H}/\partial t|$) contributions in the IMAGE area during a geomagnetic storm between 7 September 2017 23:00:00 UT and 8 September 2017 01:00:00 UT. The DF electric field maxima are given both on the ground (0 km altitude) and in the ionosphere (90 km altitude) and the CF and total electric field peaks as well as $|\partial\mathbf{H}/\partial t|$ peaks only on the ground. The CF and total electric field maxima have been determined using the denser ($0.03^\circ \times 0.07^\circ$) PGIEM2G grid and the rest using the sparser ($0.5^\circ \times 1^\circ$) SECS grid.

Contribution	UT	Geographic latitude, longitude	Amplitude
Ground $ \mathbf{E}_{DF,ext} $	7 September 2017 23:59:50	68.58°, 19.00°	4100 mV/km
Ground $ \mathbf{E}_{DF,int} $	8 September 2017 00:30:00	66.00°, 12.00°	3950 mV/km
Ground $ \mathbf{E}_{DF} = \mathbf{E}_{DF,ext} + \mathbf{E}_{DF,int} $	7 September 2017 23:15:30	67.50°, 21.00°	3753 mV/km
Ground $ \mathbf{E}_{CF} $	7 Sep 2017 23:59:50	64.54°, 11.91°	70961 mV/km
Ground $ \mathbf{E} = \mathbf{E}_{CF} + \mathbf{E}_{DF} $	7 Sep 2017 23:59:50	64.54°, 11.91°	72861 mV/km
Ground $ \partial\mathbf{H}_{ext}/\partial t $	7 September 2017 23:50:50	67.50°, 22.00°	17.52 nT/s
Ground $ \partial\mathbf{H}_{int}/\partial t $	8 September 2017 00:03:30	66.00°, 27.00°	26.96 nT/s
Ground $ \partial\mathbf{H}_{tot}/\partial t $	7 September 2017 23:50:50	68.00°, 24.00°	38.65 nT/s
Ionospheric $ \mathbf{E}_{DF,ext} $	7 September 2017 23:15:30	67.50°, 24.00°	6128 mV/km
Ionospheric $ \mathbf{E}_{DF,int} $	8 September 2017 00:29:50	66.00°, 12.00°	2897 mV/km
Ionospheric $ \mathbf{E}_{DF} = \mathbf{E}_{DF,ext} + \mathbf{E}_{DF,int} $	7 September 2017 23:15:30	67.50°, 24.00°	5628 mV/km

on the ground, which is often used as a proxy for the geoelectric field (Viljanen, 1998; Viljanen et al., 2001). This proxy is based on an approximation of Faraday’s law (Eq. 8) at the Earth’s surface

$$\frac{\partial B_\theta}{\partial t} = \frac{1}{r} \frac{\partial(rE_{DF,\phi})}{\partial r} = \frac{E_{DF,\phi}}{r} + \frac{\partial E_{DF,\phi}}{\partial r} \approx \frac{E_{DF,\phi}}{R_E} \quad (42)$$

$$\frac{\partial B_\phi}{\partial t} = -\frac{1}{r} \frac{\partial(rE_{DF,\theta})}{\partial r} = -\frac{E_{DF,\theta}}{r} - \frac{\partial E_{DF,\theta}}{\partial r} \approx -\frac{E_{DF,\theta}}{R_E} \quad (43)$$

where the first half of the equations is based on the results of Section 2.1 that at the Earth’s surface $E_{DF,r} = 0$. The times and locations of the peak external, internal or total DF electric field and $|\partial\mathbf{H}/\partial t|$ values in Table 3 do not match. This demonstrates the complexity of geomagnetic induction as mentioned in Introduction. It also indicates that the drivers of the most intense geoelectric field peaks may not be exactly the same as the drivers of rapid geomagnetic variations (Juusola et al., 2023).

4.2 Space weather application

The computations of our method are carried out in the time domain, which makes the method ideal for near real-time applications. Because both the external and internal part of the DF electric field are derived from observations, there is no need for time integration, unlike in 3-D induction modelling. Only two epochs of observations, the present and preceding epoch, are required to derive the DF electric field for the present epoch. The DF electric field computation based on the SECS method is



relatively light, as is the CF electric field estimation using Eq. 33–34. Because only $\partial B/\partial t$ and not B is needed, a baseline estimate is not necessary, making the calculation more straightforward.

Because of the assumed linear dependence of the CF electric field on the DF electric field, it is possible to determine the direction of the driving DF field for which the electric field amplitude at a given location maximizes

$$E_x = k_{xx}E_{DF,x} + k_{xy}E_{DF,y} + E_{DF,x} \quad (44)$$

$$E_y = k_{yx}E_{DF,x} + k_{yy}E_{DF,y} + E_{DF,y} \quad (45)$$

$$E_{DF,x} = |\mathbf{E}_{DF}| \cos \alpha \quad (46)$$

$$E_{DF,y} = |\mathbf{E}_{DF}| \sin \alpha \quad (47)$$

$$|\mathbf{E}| = |\mathbf{E}_{DF}| \sqrt{(k_{xx} \cos \alpha + k_{xy} \sin \alpha + \cos \alpha)^2 + (k_{yx} \cos \alpha + k_{yy} \sin \alpha + \sin \alpha)^2} \quad (48)$$

Figure 18 shows maps of the maximum (top left) and minimum $|\mathbf{E}|/|\mathbf{E}_{DF}|$ (top right), and the angle α of maximum $|\mathbf{E}|/|\mathbf{E}_{DF}|$ (bottom). The value of $|\mathbf{E}|/|\mathbf{E}_{DF}|$ is the same for $\pm \mathbf{E}_{DF}$, which is why there is repetition in the colorbar of the bottom panel. In some areas the maximum $|\mathbf{E}|/|\mathbf{E}_{DF}|$ is greater than one, indicating that the CF field enhances the DF field, and in some areas that ratio is smaller than one, indicating that the CF field always weakens the DF field. The absolute maximum value $|\mathbf{E}|/|\mathbf{E}_{DF}| = 40.66$ in the area takes place at 64.48° and 11.77° longitude, and occurs when the DF electric field angle is $\alpha = -52^\circ$, i.e., the field is directed perpendicular to the nearby coastline, where there are large conductance gradients. The condition that the derivative of Eq. 48 with respect to α is zero is repeated at intervals of $\pi/2$, indicating that the minimum $|\mathbf{E}|/|\mathbf{E}_{DF}|$ occurs when the DF field is perpendicular to the direction of the maximum enhancement. In most areas the minimum $|\mathbf{E}|/|\mathbf{E}_{DF}|$ is close to one, i.e., the CF part is close to zero and the DF part determines the electric field amplitude. Fig. 18c emphasizes the active role of the passive Earth in generating geoelectric field peaks.

4.3 Simplified models

The local 1-D (variations only in the vertical direction) model is the simplest method for estimating the electric field from magnetic field. According to the model

$$E_x(\omega) = \frac{Z(\omega)}{\mu_0} B_y(\omega) \quad (49)$$

$$E_y(\omega) = -\frac{Z(\omega)}{\mu_0} B_x(\omega), \quad (50)$$

where $Z(\omega)$ is the plane wave surface impedance of the layered Earth. It is defined by the thicknesses and electromagnetic parameters of the layers. Although the model apparently assumes that there are no lateral variations either in the conductivity or the fields, applying it locally, with local 1-D Earth models together with local magnetic field, has been shown to produce quite good results (Viljanen et al., 2004, 2012, 2014), but generally 3-D models should be preferred (A. Kelbert, 2020). The 1-D approximation of the electric field does not consider charges, which means that it is an estimate of the DF electric field.

During a geomagnetic storm, the DF electric field is generally intense and its direction varies constantly. 3-D electric field data is not always available, although DF electric field data or the $\partial \mathbf{H}/\partial t$ proxy may be. This is particularly the case for



historical events, during which magnetometer observations were very sparse. According to Eq. 48, electric field values at a given location during two events, such as two geomagnetic storms, can be compared at the times when the DF electric field has the same direction (α) during both events

$$\frac{|\mathbf{E}(t, \theta, \phi)|}{|\mathbf{E}(t_0, \theta, \phi)|} = \frac{|\mathbf{E}_{DF}(t, \theta, \phi)|}{|\mathbf{E}_{DF}(t_0, \theta, \phi)|}, \quad (51)$$

where t is a time step of the examined storm and t_0 is a time step of the bench mark storm. Near dominant conductivity gradient structures, the maximum electric field during a storm at a given location is likely to occur when the DF electric field direction is optimal for field enhancement (Fig. 18). In such a case, the peak electric field value can be obtained from the known bench mark event value by comparing the DF electric field amplitudes of the two events.

4.4 DF electric field in the ionosphere

DF electric field in the ionosphere is typically ignored although in some dynamical situations inductive effects are not negligible and the ionospheric electric field is not a pure CF field, but has a significant DF part (Vanhamäki et al., 2007; Madelaire et al., 2024). The method used to estimate the DF electric field is valid at and above the Earth's surface. Hence, it can be used to estimate the DF electric field due to telluric and DF horizontal ionospheric currents in the ionosphere as well. The resulting DF electric field is not the total DF electric field above the ionospheric horizontal current sheet, because the contribution from the CF horizontal ionospheric currents and field-aligned currents is missing. Below and at the ionospheric horizontal current sheet, this part of the DF electric field is zero because the combined magnetic field from the horizontal CF currents and (radial) field-aligned currents is zero (Fukushima, 1976; Amm, 1997). Moreover, Vanhamäki et al. (2007) argue that the DF electric field due to the CF horizontal and field-aligned currents should be very small.

Figure 19 shows the external (left), internal (middle), and total (right) DF electric field in the ionosphere at 90 km altitude on 7 September 2017 at 23:16:00 UT (top) and at 23:52:00 UT (bottom). Similar to the ground (Fig. 3 and Fig. 4), the external and internal part of the DF electric field are more or less oppositely directed, but whereas on the ground the amplitudes of the external and internal parts were almost equal, in the ionosphere the external part has a clearly stronger amplitude than the internal part. The internal part is also clearly smoother in the ionosphere than on the ground. Nonetheless, the internal part significantly modifies both the pattern and amplitude of the resulting total DF electric field, indicating that ground induction should be included when ionospheric induction is considered. The maximum amplitudes of the total DF electric field, indicated below the scale arrows in Fig. 19, have similar values as the commonly observed ionospheric situations modelled by Vanhamäki et al. (2007).

Vanhamäki et al. (2005) used the 1-D complex image method (CIM) to estimate that the electric field caused by the Earth's induction is relatively small (at most 400 mV/km) and smooth at the ionospheric altitude. This is not in agreement with our result, and indicates that the simple 1-D CIM modelling may not be sufficient for the task.

The bottom part of Table 3 shows the times, locations, and amplitudes of the maximum ionospheric DF electric field contributions in the IMAGE area during a geomagnetic storm between 7 September 2017 23:00:00 UT and 8 September 2017 01:00:00 UT. The largest external and total DF electric field both occurred at the same time and location, on 7 September 2017



at 23:15:30 UT. This was the same time when the DF total electric field maximum occurred on the ground as well. The internal DF electric field had its maximum almost at the same time both in the ionosphere and on the ground.

The method for deriving the CF electric field from known conductance and vertical current distributions derived in Section 2.2 can also be applied to the ionosphere. In that case, the ground conductance Σ is replaced by Pedersen conductance Σ_P and
 485 terms for the Hall conductance need to be added

$$\mathbf{J} = \Sigma_P \mathbf{E} + \Sigma_H \mathbf{E} \times \hat{\mathbf{e}}_r \quad (52)$$

$$\nabla \cdot \mathbf{J} = \nabla \Sigma_P \cdot (\mathbf{E}_{CF} + \mathbf{E}_{DF}) + \Sigma_P \nabla \cdot \mathbf{E}_{CF} + \nabla \Sigma_H \cdot [(\mathbf{E}_{CF} + \mathbf{E}_{DF}) \times \hat{\mathbf{e}}_r] + \Sigma_H (\nabla \times \mathbf{E}_{DF})_r \quad (53)$$

$$(\nabla \times \mathbf{J})_r = [\nabla \Sigma_P \times (\mathbf{E}_{CF} + \mathbf{E}_{DF})]_r + \Sigma_P (\nabla \times \mathbf{E}_{DF})_r + [\nabla \Sigma_H \times ((\mathbf{E}_{CF} + \mathbf{E}_{DF}) \times \hat{\mathbf{e}}_r)]_r - \Sigma_H (\nabla \cdot \mathbf{E}_{CF}). \quad (54)$$

Eq. 52 is the Ohm's law in a thin-sheet ionosphere, Eq. 53 is the ionospheric equivalent of Eq. 20, and Eq. 54 is a similar
 490 expression for the curl of the horizontal current. If \mathbf{E}_{DF} is estimated to be insignificant compared to \mathbf{E}_{CF} , Eq. 53 becomes the traditional problem of the electrostatic ionosphere of global magnetosphere-ionosphere simulations, where \mathbf{E}_{CF} is solved from known conductance and vertical current distributions. Although \mathbf{E}_{DF} is typically ignored, it would be possible to include it in the calculation, by first using Ohm's law to derive an expression for $I_{DF}(t)$ as a function of the SECS amplitudes $Q_{CF}(t)$, $I_{CF}(t)$ and $I_{DF}(t - \Delta t)$ and inserting this into Eq. 53 to obtain an equation for $Q_{CF}(t)$ in terms of the known
 495 $I_{CF}(t)$ and $I_{DF}(t - \Delta t)$. This approach resembles the inductive ionosphere solver presented by Vanhamäki (2011). Ground-based magnetometer networks can be used to determine $(\nabla \times \mathbf{J})_r$ and \mathbf{E}_{DF} , but obtaining Σ_P and Σ_H is challenging. If they could be estimated, for example from all-sky camera images, Eq. 54 would yield \mathbf{E}_{CF} . This approach resembles otherwise the corresponding solver suggested by Vanhamäki (2011), except that \mathbf{E}_{DF} would be directly obtained from ground-based magnetometer data and, thus, no time-integration would be needed.

500 4.5 Permittivity of the ground

We have used the vacuum permittivity ϵ_0 in Eq. 24 although the permittivity of the ground differs from that of the vacuum. However, this is not expected to affect the modelling of the CF electric field. The CF electric field \mathbf{E}_{CF} corresponds to all charges, including both "free" charges and polarization charges. If these are known, the electric field is calculated as an integral over this charge density, using ϵ_0 , and the dielectric properties of the material are "embedded" in the charges. The values Q_i/ϵ_0
 505 we solve for using Eq. 24 correspond to such a case. Only in the case that we were interested in separating the free charges and polarization charges, would we need to know the true permittivity distribution of the ground, and replace ϵ_0 with ϵ . However, this is not necessary when modelling the CF electric field.

5 Conclusions

We have developed a new method for estimating various contributions to the 3-D geoelectric field at the Earth's surface. The
 510 surface electric field consists of an external DF electric field due to time-varying ionospheric and magnetospheric currents, an



internal DF electric field due to time-varying telluric currents, and a CF electric field due to charge accumulation at ground conductivity gradients.

1. The external part of the DF electric field is calculated from the time derivative of the external part of the observed ground magnetic field using DF 2-D SECSs.
- 515 2. The internal part of the DF electric field is calculated from the time derivative of internal part of the observed ground magnetic field using DF 2-D SECSs.
3. The surface CF electric field is calculated from the known surface DF electric field and coefficients that linearly relate the DF electric field to the CF electric field. The coefficients were obtained from the PGIEM2G model.
4. The calculations are carried out in the time domain and only two consecutive time steps of the observed magnetic field
520 are needed to compute the surface electric field. The external part of the DF electric field is valid everywhere, the internal part at and above the Earth's surface, and the CF part at the Earth's surface. A dense magnetometer networks is required for good results.
5. The external and internal parts of the DF electric field are generally oppositely directed and have comparable amplitudes both on the ground and in the ionosphere, indicating that both contributions are significant for the total DF electric field. The largest peaks in the total DF electric field tend to occur when either the external or internal contribution is
525 temporarily suppressed at the location of interest.
6. At a given location, a DF electric field with a given amplitude can result in a total surface electric field amplitude with an orders of magnitude difference depending on the direction of the DF electric field with respect to the locally dominant conductivity gradient structure.
- 530 7. Peak amplitudes of the various electric field contributions did not occur at the same time or at the same location as the peak amplitudes of the time derivative of the horizontal magnetic field for our example event. This indicates that analysis of rapid magnetic field variations may not describe all relevant aspects of the electric field behaviour.
8. The linear dependence of the DF electric field on $\partial B/\partial t$ observations on the one hand, and of the CF electric field on the DF electric field on the other hand, makes it possible to estimate the total geoelectric field directly from nearby magnetic field observations. As an example, we have determined coefficients that relate the geoelectric field -driven GIC at MAN
535 to NUR $\partial B/\partial t$.

Analysing the separated contributions from currents (DF electric field) and charges (CF electric field) to the geoelectric field can help in clarifying the complicated interaction between the ionosphere and the conducting ground.

540 *Code and data availability.* IMAGE data (Juusola et al., 2024) are available at <https://space.fmi.fi/image>. The code for the SECS method is available in Vanhamäki and Juusola (2020). The code used to calculate magnetic coordinates and local times (Laundal et al., 2022)



is available at <https://apexpy.readthedocs.io/en/latest/>. PGIEM2G 3-D EM forward modeling code is developed openly at Gitlab (<https://gitlab.com/m.kruglyakov/PGIEM2G>) and available under GPLv2. The geomagnetic north and east components of the observed geoelectric field downsampled to 10 seconds (Kruglyakov and Marshalko, 2023) are available at <https://zenodo.org/records/8402165>. GIC data (Viljanen, 2023) are available at <https://space.fmi.fi/gic>. The coefficients relating the CF electric field to the DF electric field (Eq. 33–34, Fig. 9–10) are
545 provided as supplementary material.

Author contributions. LJ implemented the method and prepared the manuscript, HV carried out the PGIEM2G electric field separation into CF and DF parts, and EM provided the PGIEM2G data. MK is the author of PGIEM2G and provided expert advice on geoelectric field modelling. AV provided expert advice on the physics of geomagnetic induction. All co-authors participated in writing the manuscript.

Competing interests. The authors declare that they have no conflict of interest.

550 *Acknowledgements.* We thank the institutes who maintain the IMAGE Magnetometer Array: Tromsø Geophysical Observatory of UiT the Arctic University of Norway (Norway), Finnish Meteorological Institute (Finland), Institute of Geophysics Polish Academy of Sciences (Poland), GFZ German Research Centre for Geosciences (Germany), Geological Survey of Sweden (Sweden), Swedish Institute of Space Physics (Sweden), Sodankylä Geophysical Observatory of the University of Oulu (Finland), Polar Geophysical Institute (Russia), DTU Technical University of Denmark (Denmark), and Science Institute of the University of Iceland (Iceland). The provisioning of data from AAL,
555 GOT, HAS, NRA, VXJ, FKP, ROE, BFE, BOR, HOV, SCO, KUL, and NAQ is supported by the ESA contracts number 4000128139/19/D/CT as well as 4000138064/22/D/KS. GIC data were recorded in collaboration with Gasum Oy. This research was supported by the Academy of Finland project no. 339329 and no. 354521. MK was supported by the New Zealand Ministry of Business, Innovation, Employment through Endeavour Fund Research Programme contract UOOX2002.



References

- 560 A. Kelbert, A.: The Role of Global/Regional Earth Conductivity Models in Natural Geomagnetic Hazard Mitigation, *Surv. Geophys.*, 41:115, <https://doi.org/https://doi.org/10.1007/s10712-019-09579-z>, 2020.
- Amm, O.: Ionospheric elementary current systems in spherical coordinates and their application, *J. Geomagn. Geoelectr.*, 49, 947–955, <https://doi.org/https://doi.org/10.5636/jgg.49.947>, 1997.
- Amm, O. and Viljanen, A.: Ionospheric disturbance magnetic field continuation from the ground to ionosphere using spherical elementary
565 current systems, *Earth Planets Space*, 51, 431–440, <https://doi.org/https://dx.doi.org/10.1186/BF03352247>, 1999.
- Dimmock, A. P., Rosenqvist, L., Hall, J.-O., Viljanen, A., Yordanova, E., Honkonen, I., André, M., and Sjöberg, E. C.: The GIC and geomagnetic response over Fennoscandia to the 7–8 September 2017 geomagnetic storm, *Space Weather*, 17, 989–1010, <https://doi.org/https://doi.org/10.1029/2018SW002132>, 2019.
- Emmert, J. T., Richmond, A. D., and Drob, D. P.: A computationally compact representation of Magnetic-Apex and Quasi-Di pole coordinates
570 with smooth base vectors, *J. Geophys. Res.*, 115, A08322, <https://doi.org/https://doi.org/10.1029/2010JA015326>, 2010.
- Fukushima, N.: Generalized theorem for no ground magnetic effect of vertical currents connected with Pedersen currents in the uniform-conductivity ionosphere, *Rep. Ionos. Space. Res. Japan*, 30, 35–40, 1976.
- Jackson, J. D.: *Classical Electrodynamics*, 3rd Edition, Wiley, 1998.
- Juusola, L., Kauristie, K., Vanhamäki, H., and Aikio, A.: Comparison of auroral ionospheric and field-aligned currents derived from Swarm and ground magnetic field measurements, *J. Geophys. Res. Space Physics*, 121, 9256–9283,
575 <https://doi.org/https://doi.org/10.1002/2016JA022961>, 2016.
- Juusola, L., Vanhamäki, H., Viljanen, A., and Smirnov, M.: Induced currents due to 3D ground conductivity play a major role in the interpretation of geomagnetic variations, *Ann. Geophys.*, 38, 983–998, <https://doi.org/https://doi.org/10.5194/angeo-38-983-2020>, 2020.
- Juusola, L., Viljanen, A., Dimmock, A. P., Kellinsalmi, M., Schillings, A., and Weygand, J. M.: Drivers of rapid geomagnetic variations at
580 high latitudes, *Ann. Geophys.*, 41, 13–37, <https://doi.org/https://doi.org/10.5194/angeo-41-13-2023>, 2023.
- Juusola, L., Björnsson, G., Johnsen, M. G., Kauristie, K., Kellinsalmi, M., Matzka, J., Neska, A., Raita, T., Reda, J., Tanskanen, E., Viljanen, A., Willer, A. N., Wittke, J., and Yamauchi, M.: International Monitor for Auroral Geomagnetic Effects (IMAGE) [data set], <https://space.fmi.fi/image>, last access: September 10, 2024, 2024.
- Kelbert, A., Balch, C. C., Pulkkinen, A., Egbert, G. D., Love, J. J., Rigler, E. J., and Fujii, I.: Methodology for time-domain estimation of storm time geoelectric fields using the 3-D magnetotelluric response tensors, *Space Weather*, 15, 874–894,
585 <https://doi.org/https://doi.org/10.1002/2017SW001594>, 2017.
- Kellinsalmi, M., Viljanen, A., Juusola, L., and Käki, S.: The time derivative of the geomagnetic field has a short memory, *Ann. Geophys. Discuss.*, <https://doi.org/https://doi.org/10.5194/angeo-2022-4>, 2022.
- Korja, T., Engels, M., Zhamaletdinov, A. A., Kovtun, A. A., Palshin, N. A., Smirnov, M. Y., Tokarev, A. D., Asming, V. E., n, L. L. V., Vardaniants, I. L., and the BEAR Working Group: Crustal conductivity in Fennoscandia — a compilation of a database on crustal conductance in the Fennoscandian Shield, *Earth Planets Space*, 54, 535–558, <https://doi.org/https://doi.org/10.1186/BF03353044>, 2002.
- Kruglyakov, M. and Bloshanskaya, L.: High-performance parallel solver for integral equations of electromagnetics based on Galerkin method, *Mathematical Geosciences*, 49, 751–776, <https://doi.org/https://doi.org/10.1007/s11004-017-9677-y>, 2017.
- Kruglyakov, M. and Kuvshinov, A.: Using high-order polynomial basis in 3-D EM forward modeling based on volume integral equation
595 method, *Geophysical Journal International*, 213, 1387–1401, <https://doi.org/https://doi.org/10.1093/gji/ggy059>, 2018.



- Kruglyakov, M. and Marshalko, E.: Datasets and code for “Multi-site transfer function approach for real-time modeling of the ground electric field induced by laterally-nonuniform ionospheric source” by Kruglyakov et al. (2023) [data set], Zenodo <https://doi.org/10.5281/zenodo.8402165>, last access: September 10, 2024, 2023.
- Kruglyakov, M., Kuvshinov, A., and Marshalko, E.: Real-time 3-D modeling of the ground electric field due to space weather events. A concept and its validation., *Space Weather*, 20, e2021SW002906, <https://doi.org/10.1029/2021SW002906>, 2022.
- Kruglyakov, M., Marshalko, E., and M. Smirnov, A. K., and Viljanen, A.: Multi-site transfer function approach for real-time modeling of the ground electric field induced by laterally-nonuniform ionospheric source, *Space Weather*, 21, e2023SW003621, <https://doi.org/10.1029/2023SW003621>, 2023.
- Laundal, K. M., Yee, J. H., Merkin, V. G., Gjerloev, J. W., Vanhamäki, H., Reistad, J. P., Madelaire, M., Sorathia, K., and Espy, P. J.: Electrojet estimates from mesospheric magnetic field measurements, *Journal of Geophysical Research: Space Physics*, 126, e2020JA028644, <https://doi.org/10.1029/2020JA028644>, 2021.
- Laundal, K. M., van der Meeren, C., Burrell, A. G., Starr, G., Reimer, A., Morschhauser, A., and Lamarche, L.: ApexPy [code], <https://apexpy.readthedocs.io/en/latest/>, last access: September 10, 2024, 2022.
- Love, J. J., Lucas, G. M., Kelbert, A., and Bedrosian, P. A.: Geoelectric hazard maps for the Pacific Northwest, *Space Weather*, 16, 1114–1127, <https://doi.org/10.1029/2018SW001844>, 2018.
- Lucas, G., Love, J. J., Kelbert, A., Bedrosian, P. A., and Rigler, E. J.: A 100-year geoelectric hazard analysis for the U.S. high-voltage power grid, *Space Weather*, 18, e2019SW002329, <https://doi.org/10.1029/2019SW002329>, 2020.
- Lucas, G. M., Love, J. J., and Kelbert, A.: Calculation of voltages in electric power transmission lines during historic geomagnetic storms: An investigation using realistic earth impedances, *Space Weather*, 16, 181–195, <https://doi.org/10.1002/2017SW001779>, 2018.
- Madelaire, M., Laundal, K., Hatch, S., Vanhamäki, H., Reistad, J., Ohma, A., Merkin, V., and Lin, D.: Estimating the ionospheric induction electric field using ground magnetometers, *Geophysical Research Letters*, 51, e2023GL105443, <https://doi.org/10.1029/2023GL105443>, 2024.
- Malone-Leigh, J., Campaña, J., Gallagher, P. T., Neukirch, M., Hogg, C., and Hodgson, J.: Nowcasting geoelectric fields in Ireland using magnetotelluric transfer functions, *J. Space Weather Space Clim.*, 13, <https://doi.org/10.1051/swsc/2023004>, 2023.
- Marsal, S., Torta, J. M., Segarra, A., and Araki, T.: Use of spherical elementary currents to map the polar current systems associated with the geomagnetic sudden commencements on 2013 and 2015 St. Patrick’s Day storms, *J. Geophys. Res. Space Physics*, 122, 194–211, <https://doi.org/10.1002/2016JA023166>, 2017.
- Marsal, S., Torta, J. M., Pavón-Carrasco, F. J., Blake, S. P., and Piersanti, M.: Including the temporal dimension in the SECS technique, *Space Weather*, 18, e2020SW002491, <https://doi.org/10.1029/2020SW002491>, 2020.
- Marshalko, E., Kruglyakov, M., Kuvshinov, A., Juusola, L., Kwagala, N. K., Sokolova, E., and Pilipenko, V.: Comparing three approaches to the inducing source setting for the ground electromagnetic field modeling due to space weather events, *Space Weather*, 19, e2020SW002657, <https://doi.org/10.1029/2020SW002657>, 2021.
- Marshalko, E., Kruglyakov, M., Kuvshinov, A., and Viljanen, A.: Three-dimensional modeling of the ground electric field in Fennoscandia during the Halloween geomagnetic storm, *Space Weather*, 21, e2022SW003370, <https://doi.org/10.1029/2022SW003370>, 2023.
- McLay, S. A. and Beggan, C. D.: Interpolation of externally-caused magnetic fields over large sparse arrays using Spherical Elementary Current Systems, *Ann. Geophys.*, 28, 1795–1805, <https://doi.org/10.5194/angeo-28-1795-2010>, 2010.



- Pulkkinen, A., Viljanen, A., Pajunpää, K., and Pirjola, R.: Recordings and occurrence of geomagnetically induced currents in the Finnish natural gas pipeline network, *Journal of Applied Geophysics*, 48, 219–231, [https://doi.org/https://doi.org/10.1016/S0926-9851\(01\)00108-2](https://doi.org/https://doi.org/10.1016/S0926-9851(01)00108-2), 2001.
- Pulkkinen, A., Amm, O., Viljanen, A., and BEAR Working Group: Ionospheric equivalent current distributions determined with the method of spherical elementary current systems, *J. Geophys. Res.*, 108(A2), <https://doi.org/https://doi.org/10.1029/2001JA005085>, 2003a.
- Pulkkinen, A., Amm, O., Viljanen, A., and BEAR Working Group: Separation of the geomagnetic variation field on the ground into external and internal parts using the spherical elementary current system method, *Earth, Planets and Space*, 55, 117–129, <https://doi.org/https://doi.org/10.1186/BF03351739>, 2003b.
- Pulkkinen, A., Bernabeu, E., Thomson, A., Viljanen, A., Pirjola, R., Boteler, D., Eichner, J., Cilliers, P. J., Welling, D., Savani, N. P., Weigel, R. S., Love, J. J., Balch, C., Ngwira, C. M., Crowley, G., Schultz, A., Kataoka, R., Anderson, B., Fugate, D., Simpson, J. J., and MacAlester, M.: Geomagnetically induced currents: Science, engineering, and applications readiness, *Space Weather*, 15, 828–856, <https://doi.org/https://doi.org/10.1002/2016SW001501>, 2017.
- Richmond, A. D.: Ionospheric electrodynamics using Magnetic Apex Coordinates, *Journal of geomagnetism and geoelectricity*, 47(2), 191–212, <https://doi.org/https://doi.org/10.5636/jgg.47.191>, 1995.
- Rosenqvist, L. and Hall, J. O.: Regional 3-D modeling and verification of geomagnetically induced currents in Sweden, *Space Weather*, 17, 27–36, <https://doi.org/https://doi.org/10.1029/2018SW002084>, 2019.
- Smirnov, M., Korja, T., and Pedersen, L.: Electromagnetic Mini Array (EMMA) Project in Fennoscandia Looking Into Deep Lithosphere, in: *Proceedings of the 7th International Conference ROBLEMS OF GEOCOSMOS St. Petersburg*, Petrodvorets May, pp. 26–30, 2006.
- Vanhamäki, H.: Inductive ionospheric solver for magnetospheric MHD simulations, *Ann. Geophys.*, 29, 97–108, <https://doi.org/https://doi.org/10.5194/angeo-29-97-2011>, 2011.
- Vanhamäki, H. and Juusola, L.: Introduction to Spherical Elementary Current Systems, in: *Ionospheric Multi-Spacecraft Analysis Tools*, pp. 5–33, *ISSI Scientific Report Series 17*, <https://doi.org/https://doi.org/10.1007/978-3-030-26732-2>, 2020.
- Vanhamäki, H., Viljanen, A., and Amm, O.: Induction effects on ionospheric electric and magnetic fields, *Ann. Geophys.*, 23, 1735–1746, <https://doi.org/https://doi.org/10.5194/angeo-23-1735-2005>, 2005.
- Vanhamäki, H., Amm, O., and Viljanen, A.: Role of inductive electric fields and currents in dynamical ionospheric situations, *Ann. Geophys.*, 25, 437–455, <https://doi.org/https://doi.org/10.5194/angeo-25-437-2007>, 2007.
- Vanhamäki, H., Viljanen, A., Pirjola, R., and Amm, O.: Deriving the geomagnetically induced electric field at the Earth's surface from the time derivative of the vertical magnetic field, *Earth, Planets and Space*, 65, 997–1006, <https://doi.org/https://doi.org/10.5047/eps.2013.03.013>, 2013.
- Viljanen, A.: Relation of geomagnetically induced currents and local geomagnetic variations, in: *IEEE Transactions on Power Delivery*, vol. 13, 4, pp. 1285–1290, <https://doi.org/https://doi.org/10.1109/61.714497>, 1998.
- Viljanen, A.: GIC recordings in the Finnish natural gas pipeline [data set], <https://space.fmi.fi/gic>, last access: September 10, 2024, 2023.
- Viljanen, A., Nevanlinna, H., Pajunpää, K., and Pulkkinen, A.: Time derivative of the horizontal geomagnetic field as an activity indicator, *Ann. Geophys.*, 19, 1107–1118, <https://doi.org/https://doi.org/10.5194/angeo-19-1107-2001>, 2001.
- Viljanen, A., Pulkkinen, A., Amm, O., Pirjola, R., Korja, T., and Group, B. W.: Fast computation of the geoelectric field using the method of elementary current systems and planar Earth models, *Ann. Geophys.*, 22, 101–113, <https://doi.org/https://doi.org/10.5194/angeo-22-101-2004>, 2004.



- Viljanen, A., Pulkkinen, A., Pirjola, R., Pajunpää, K., Posio, P., and Koistinen, A.: Recordings of geomagnetically induced currents and a nowcasting service of the Finnish natural gas pipeline system, *Space Weather*, 4, <https://doi.org/https://doi.org/10.1029/2006SW000234>, 2006.
- 675 Viljanen, A., Pirjola, R., Wik, M., Ádám, A., Prácsér, E., Sakharov, Y., and Katkalov, J.: Continental scale modelling of geomagnetically induced currents, *J. Space Weather Space Clim.*, 2, A17, <https://doi.org/https://doi.org/10.1051/swsc/2012017>, 2012.
- Viljanen, A., Pirjola, R., Prácsér, E., Katkalov, J., and Wik, M. W.: Geomagnetically induced currents in Europe - Modelled occurrence in a continent-wide power grid, *J. Space Weather Space Clim.*, 4, A09, <https://doi.org/https://doi.org/10.1051/swsc/2014006>, 2014.
- Walker, S., Laundal, K., Reistad, J., Ohma, A., and Hatch, S.: Statistical temporal variations in the auroral electrojet estimated with ground magnetometers in Fennoscandia, *Space Weather*, 21, e2022SW003305, <https://doi.org/https://doi.org/10.1029/2022SW003305>, 2023.
- 680 Weygand, J. M., Amm, O., Viljanen, A., Angelopoulos, V., Murr, D., Engebretson, M. J., Gleisner, H., and Mann, I.: Application and validation of the spherical elementary currents systems technique for deriving ionospheric equivalent currents with the North American and Greenland ground magnetometer arrays, *J. Geophys. Res.*, 116, <https://doi.org/https://doi.org/10.1029/2010JA016177>, 2011.

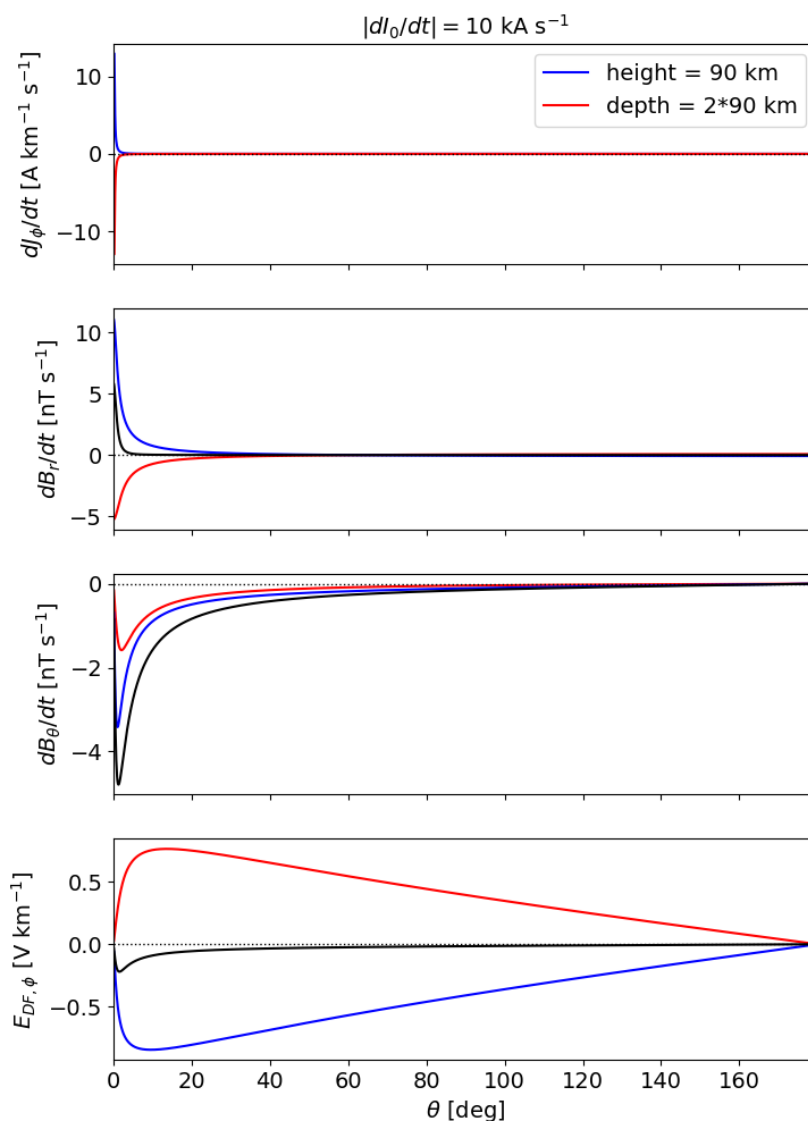


Figure 2. Co-latitude profiles of $\partial J_\phi/\partial t$, ground $\partial B_r/\partial t$, ground $\partial B_\theta/\partial t$, and ground $E_{DF,\phi}$ for two different cases: J_ϕ of a DF 2-D SECS at 90 km altitude (blue curves, external contribution) and oppositely directed J_ϕ at 2×90 km depth (red curves, internal contribution). Both have the same rate of change of the SECS amplitude $|\partial I_{DF}/\partial t| = 10$ kA/s. The sum of the external and internal $\partial B_r/\partial t$, $\partial B_\theta/\partial t$, and $E_{DF,\phi}$ on the ground are shown by the black curves.



Figure 3. External (left), internal (middle), and total (right) time derivative of the magnetic field ($\partial\mathbf{B}/\partial t$, top) and DF electric field (\mathbf{E}_{DF} , bottom) on the ground on 7 Sep 2017 at 23:16 UT. The horizontal component is shown by vectors in all plots. In the top row, the vertical component of $\partial\mathbf{B}/\partial t$ is shown by color, and in the bottom row, the curl of \mathbf{E}_{DF} . Note that the color and arrow length scales vary between panels. Locations of the IMAGE magnetometer stations used in the analysis are indicated by the black squares. Apex coordinates (Richmond, 1995; Emmert et al., 2010; Laundal et al., 2022) are indicated with the blue grid. The north, east, and down components (B_x, B_y, B_z) used in the plots correspond to $(-B_r, -B_\theta, B_\phi)$.

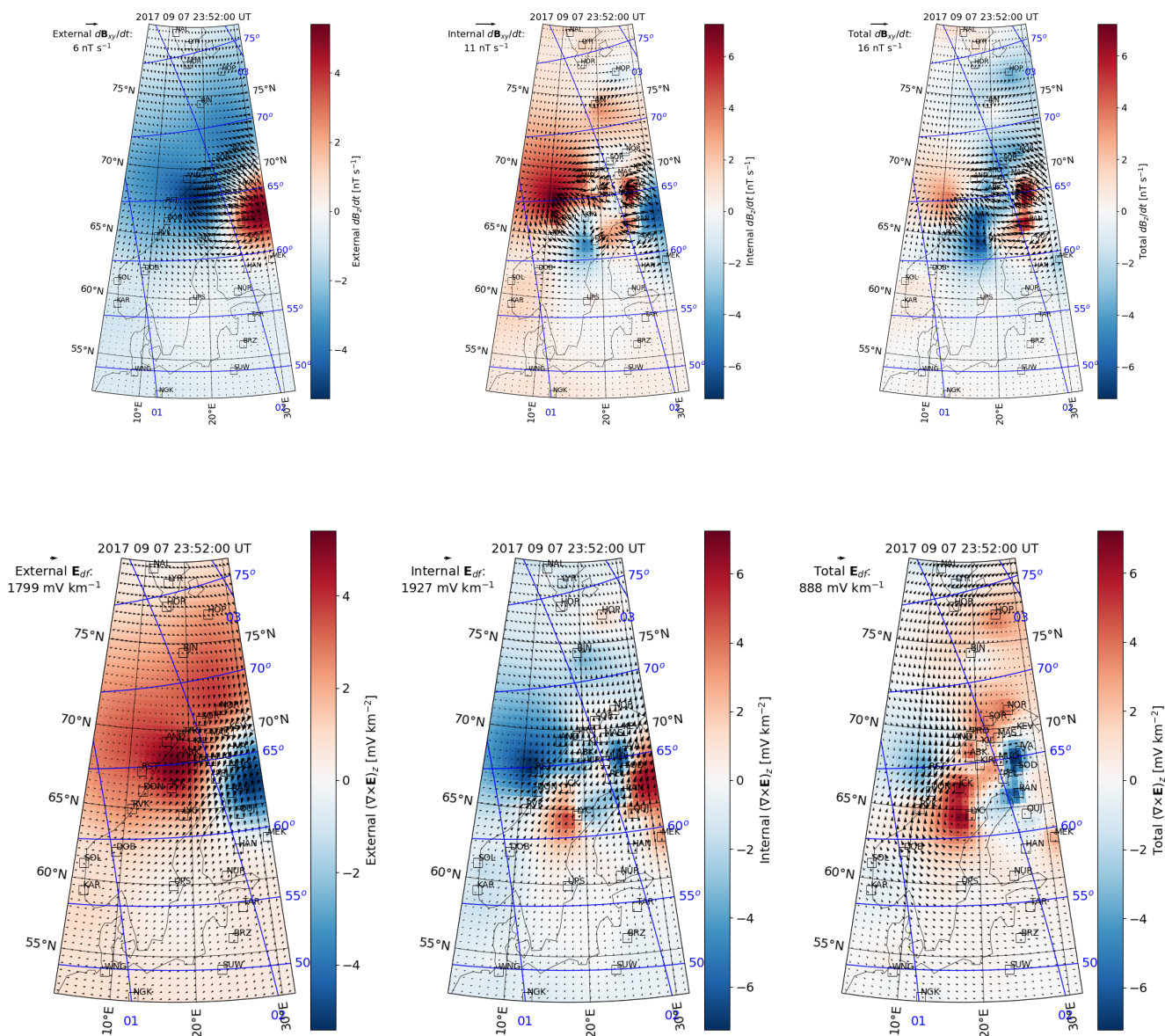


Figure 4. The same as Figure 3 except for the epoch 23:52 UT instead of 23:16 UT.

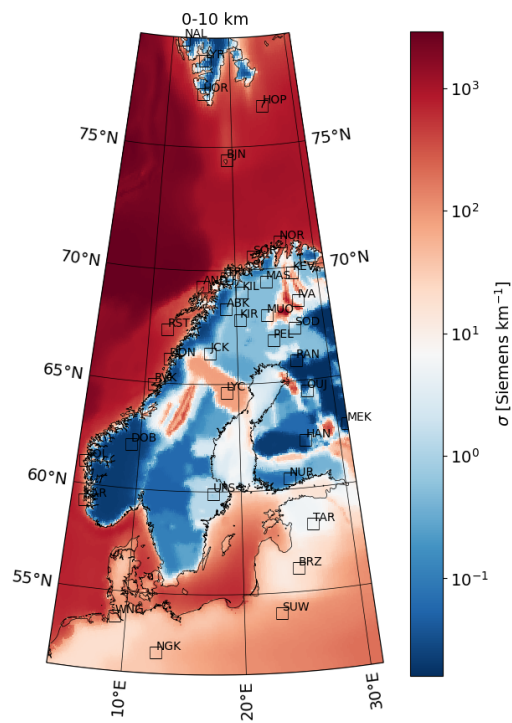


Figure 5. Conductivity in the 0–10 km layer according to the SMAP model (Korja et al., 2002).

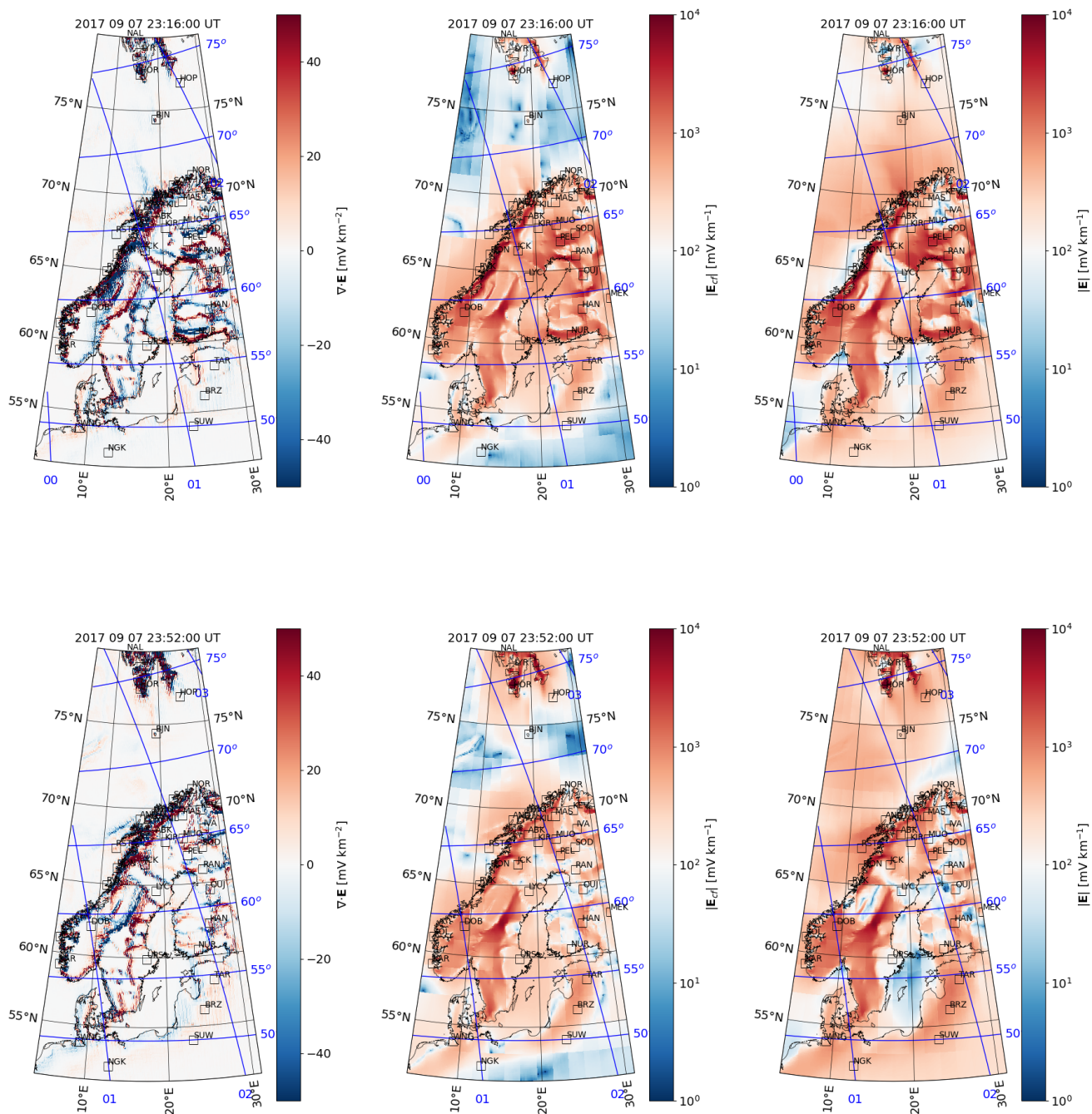
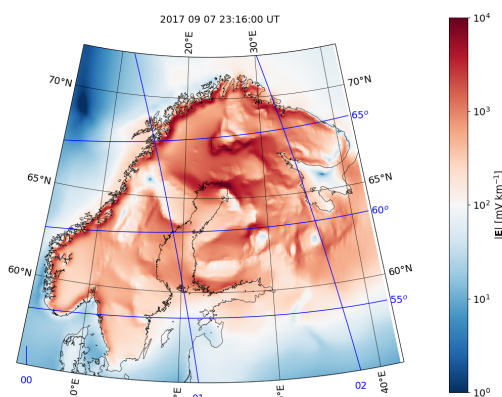


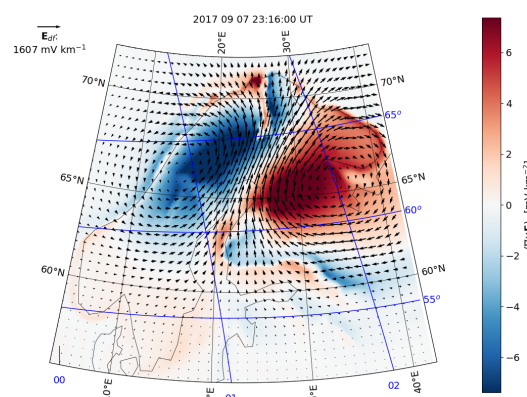
Figure 6. Divergence of the electric field (left column), horizontal CF electric field amplitude (middle column), and horizontal total electric field amplitude (right column) calculated using the SECS method with the assumption of vanishing vertical current density on 7 Sep 2017 at 23:16:00 UT (top row) and at 23:52:00 UT (bottom row).



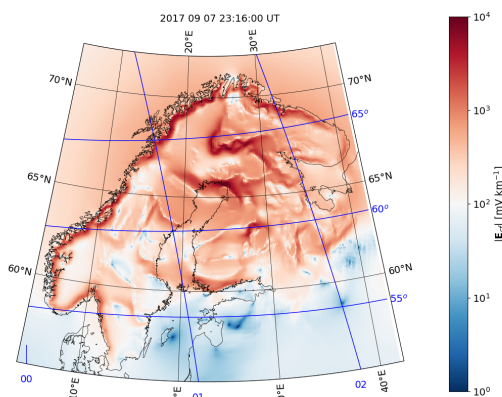
(a) PGIEM2G $|\mathbf{E}|$



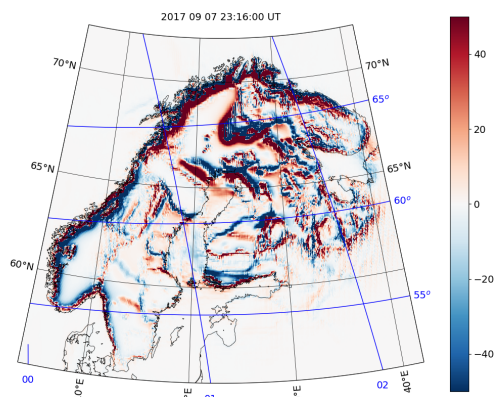
(b) PGIEM2G \mathbf{E}_{DF} and $(\nabla \times \mathbf{E})_z$



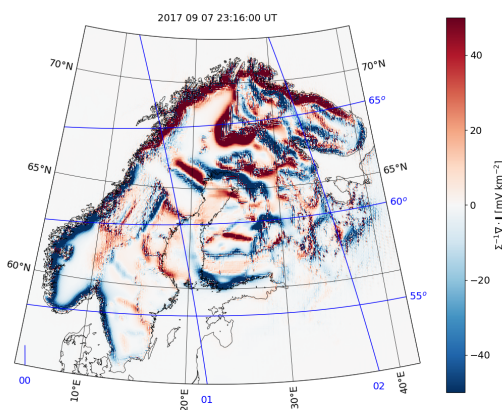
(c) PGIEM2G $|\mathbf{E}_{CF}|$



(d) PGIEM2G $\nabla \cdot \mathbf{E}$



(e) PGIEM2G $\nabla \cdot \mathbf{J} / \Sigma$



(f) SECS $\nabla \cdot \mathbf{E}$

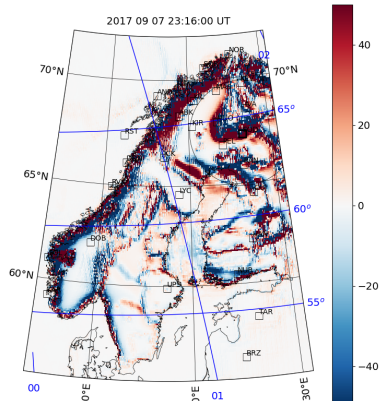




Figure 7. Horizontal electric field amplitude modelled using PGIEM2G (Marshalko et al., 2021) (top left), DF part of the electric field and its curl (arrows and color in the top right panel), CF part of the electric field (middle left), divergence of the electric field (middle right), and divergence of the horizontal current density divided by conductance (bottom left). The bottom right panel shows the divergence of the electric field derived using the SECS method when the DF electric field and radial current density are from PGIEM2G.

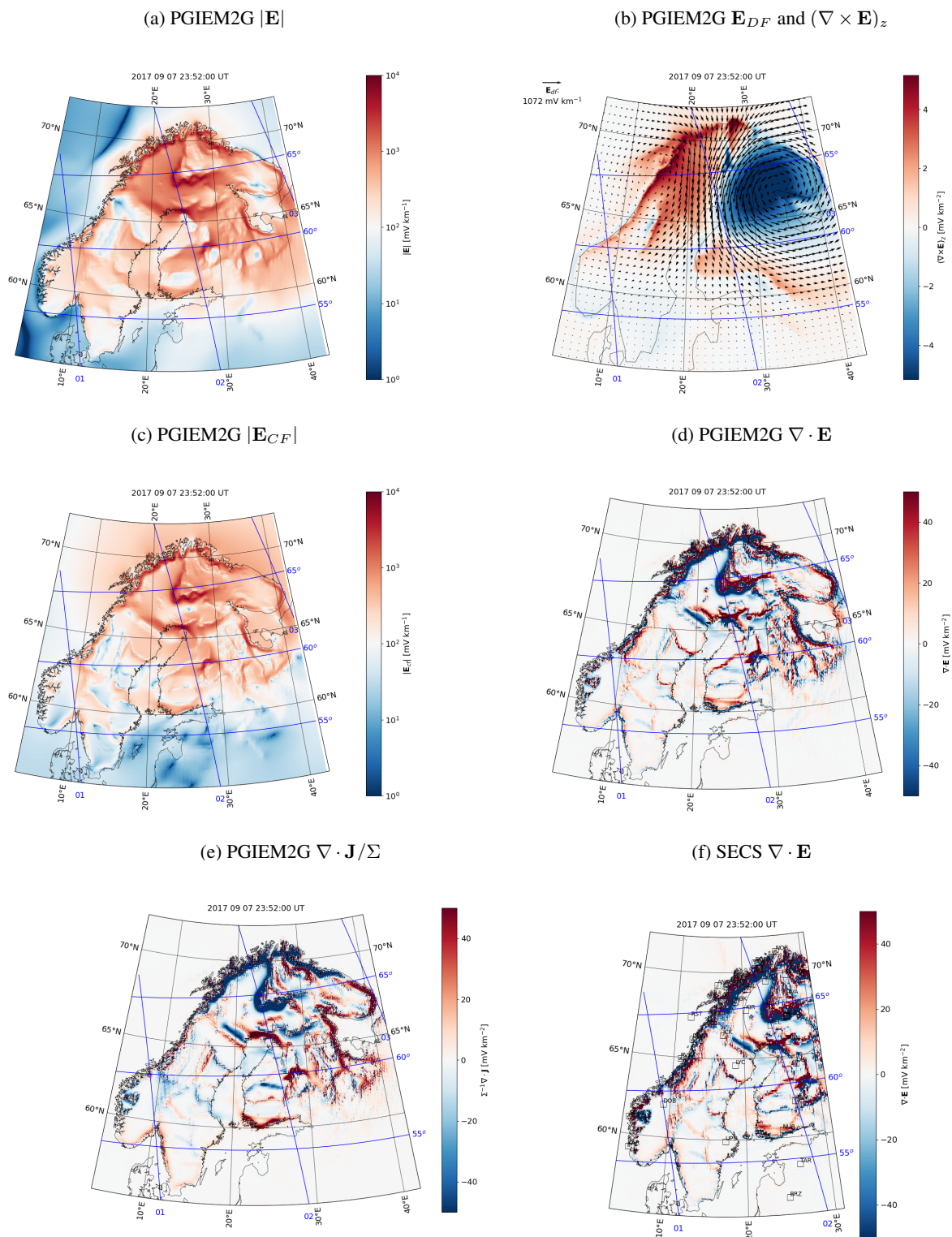


Figure 8. The same as Figure 7 except for the epoch 23:52 UT instead of 23:16 UT.

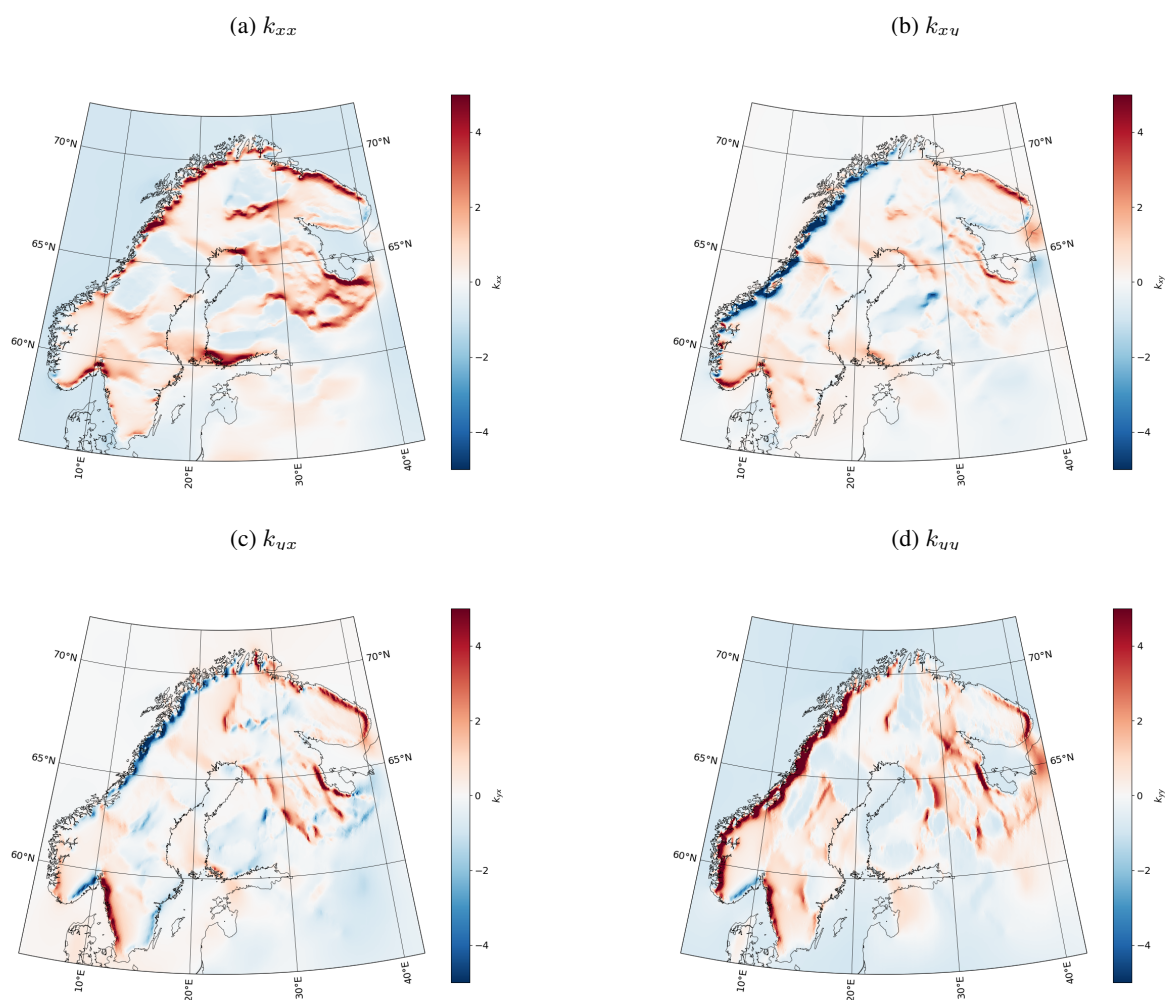


Figure 9. Proportionality coefficients (Eq. 33–34) derived using the CF and DF part of PGIEM2G’s horizontal surface electric field between 7 September 2017 23:00 UT and 8 September 2017 01:00 UT.

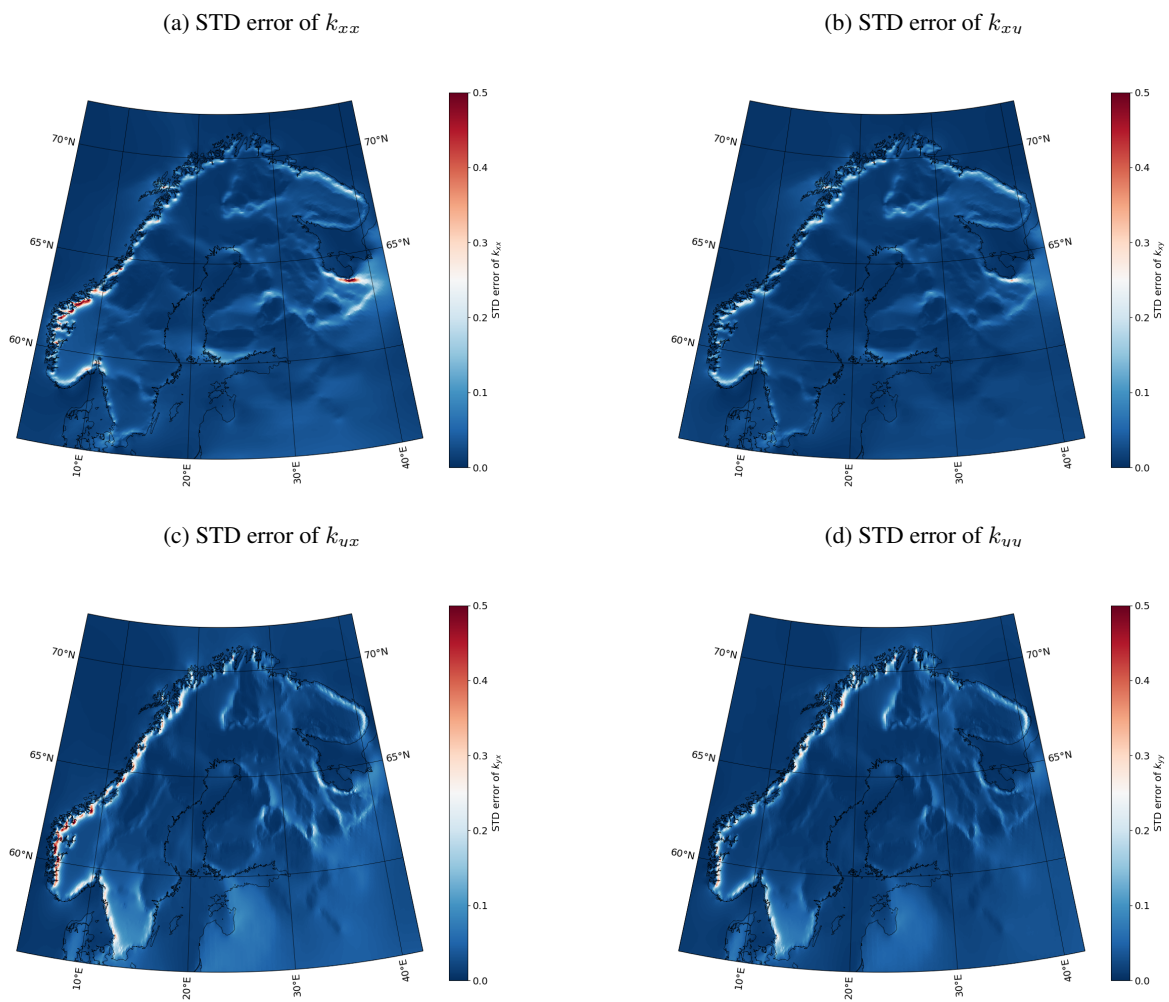


Figure 10. The same as Figure 9 except that instead of the coefficients their standard deviation (STD) errors are shown.

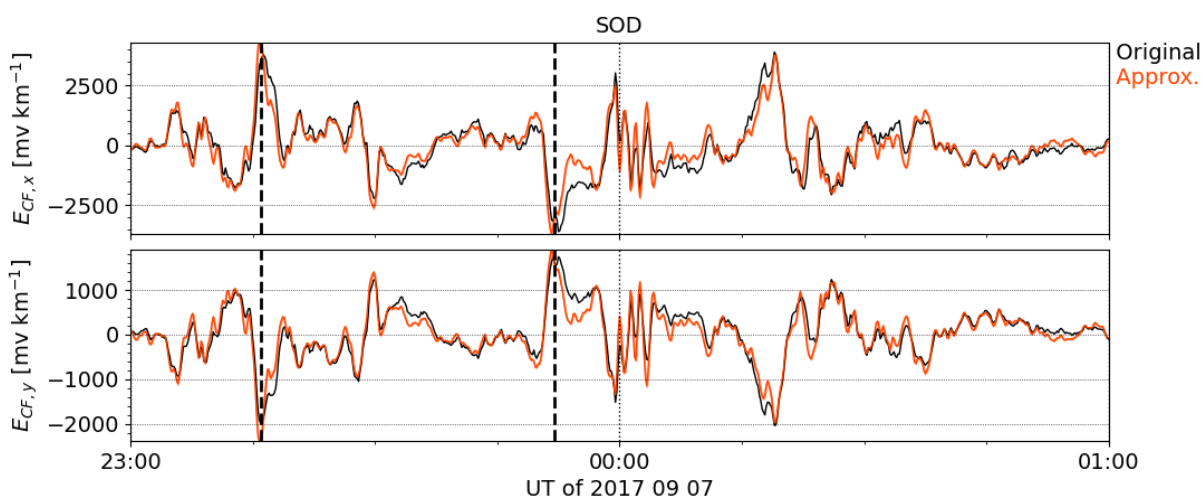
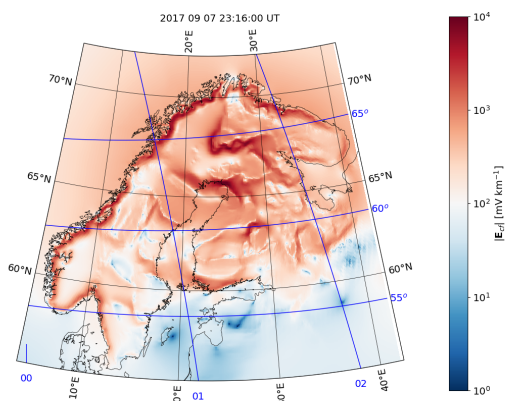


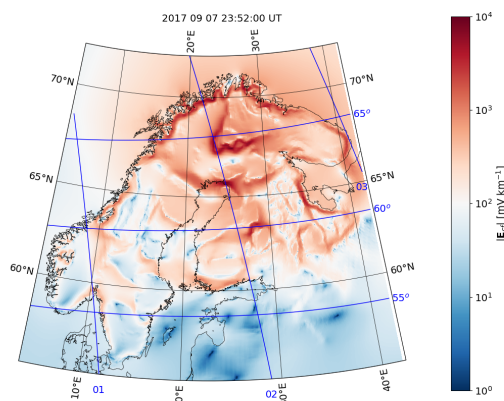
Figure 11. CF electric field at SOD between 7 September 2017 23:00 UT and 8 September 2017 01:00 UT. The original PGIEM2G-modelled value is shown in black and an approximation based on Eq. 33–34 is shown in red.



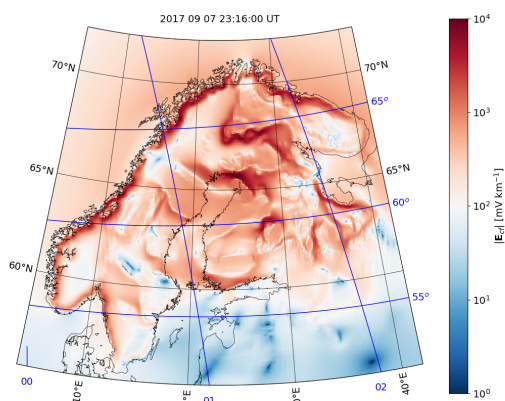
(a) Original PGIEM2G $|\mathbf{E}_{CF}|$



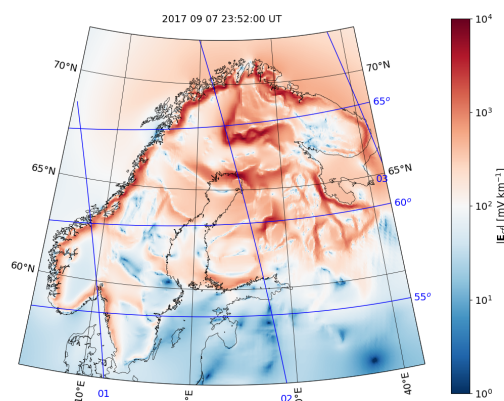
(b) Original PGIEM2G $|\mathbf{E}_{CF}|$



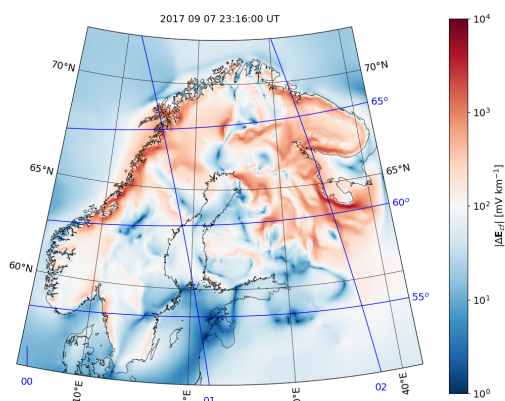
(c) Approximated $|\mathbf{E}_{CF}|$



(d) Approximated $|\mathbf{E}_{CF}|$



(e) Difference $|\Delta\mathbf{E}_{CF}|$



(f) Difference $|\Delta\mathbf{E}_{CF}|$

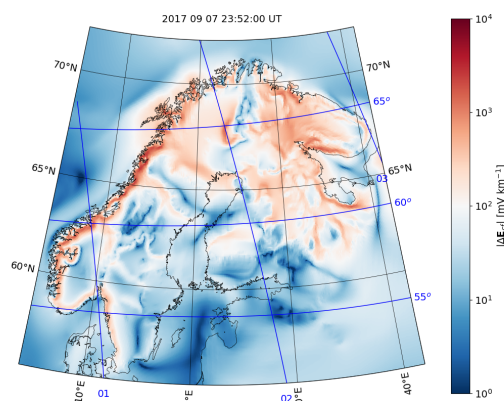




Figure 12. CF part of the horizontal electric field modelled by PGIEM2G on 7 Sep 2017 at 23:16:00 UT (left) and at 23:52:00 UT (right), CF electric field approximated using Eq. 33–34 with the coefficients from Fig. 9 and DF electric field from PGIEM2G (middle row), and the difference between the original and approximated CF field (bottom row).

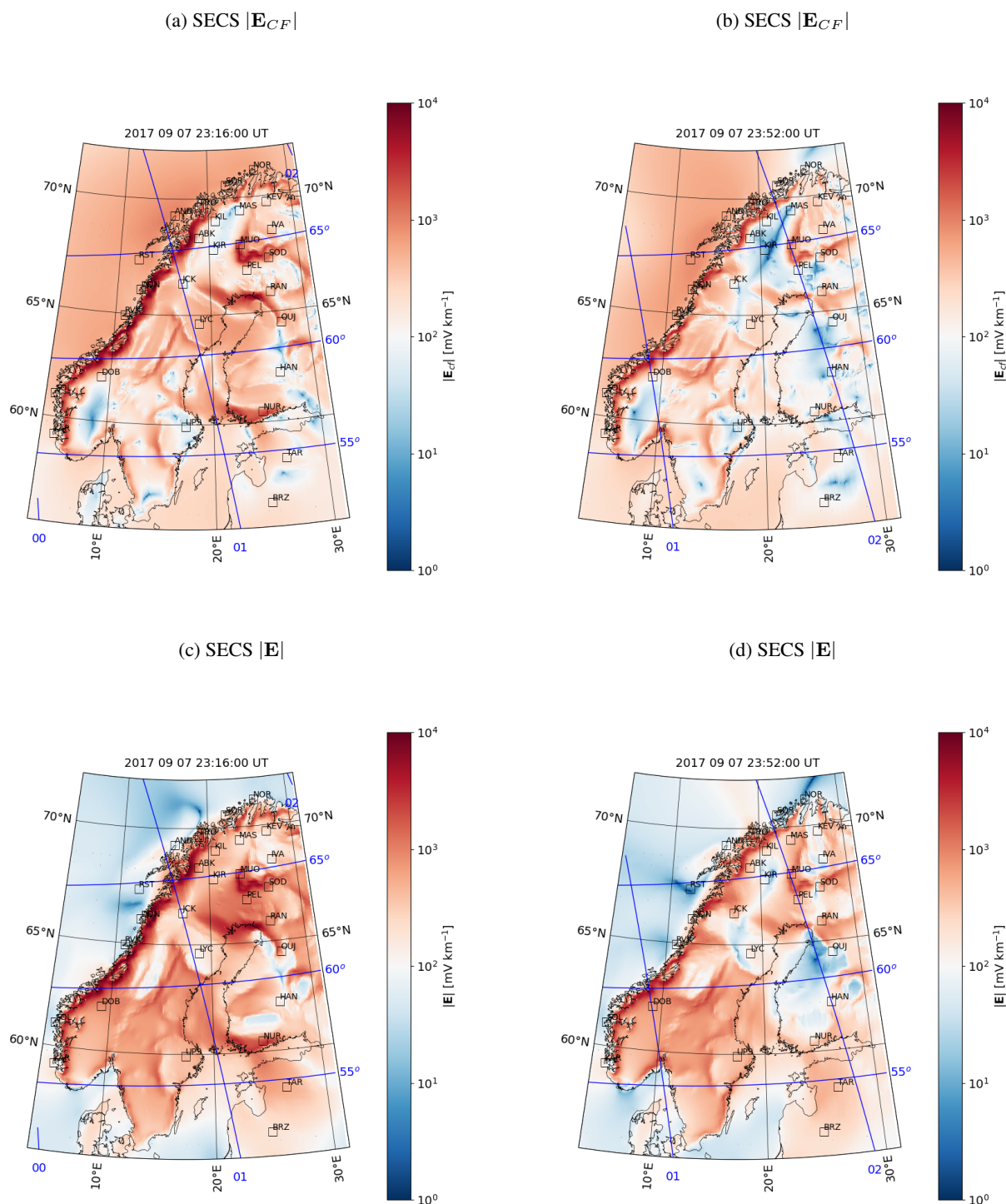


Figure 13. CF electric field (top) approximated using Eq. 33–34 with the coefficients from Fig. 9 and DF electric field from SECS on 7 Sep 2017 at 23:16:00 UT (left) and at 23:52:00 UT (right). The bottom row shows the total electric field.

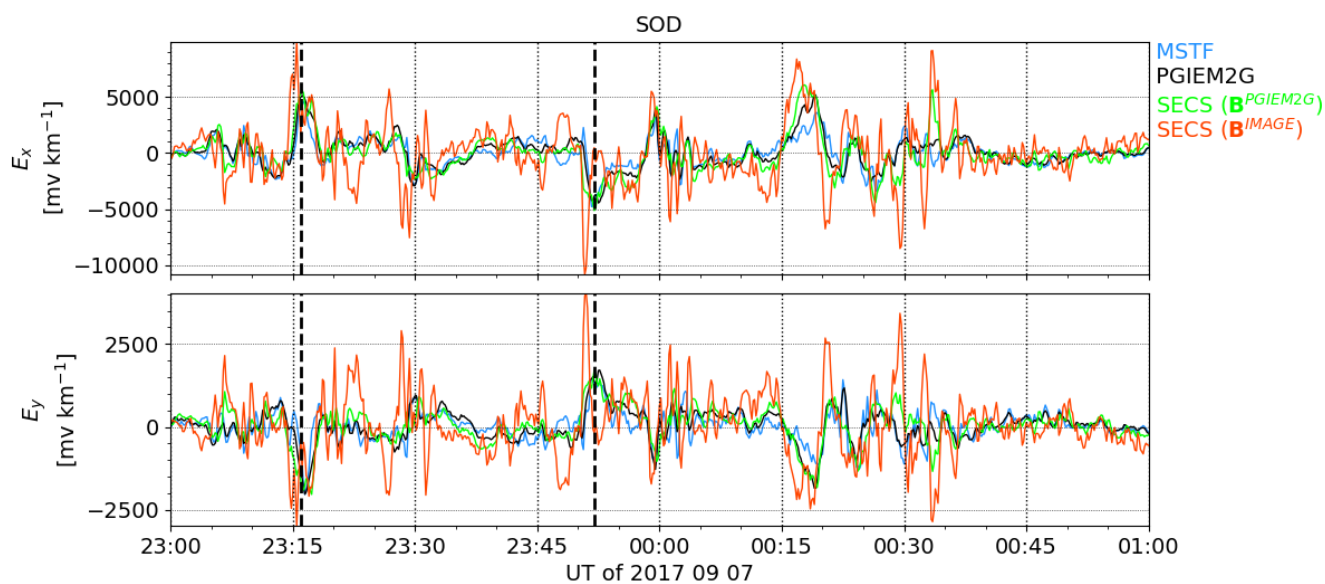


Figure 14. E_x and E_y at SOD between 7 September 2017 23:00 UT and 8 September 2017 01:00 UT. PGIEM2G modelling is shown in black and SECS (DF electric field from SECS, CF electric field from Eq. 33–34) modelling in red (calculated using the magnetic field from IMAGE) and green (calculated using the magnetic field from PGIEM2G). The multi-site transfer function (MSTF) approach (Kruglyakov et al., 2023) is shown in blue.

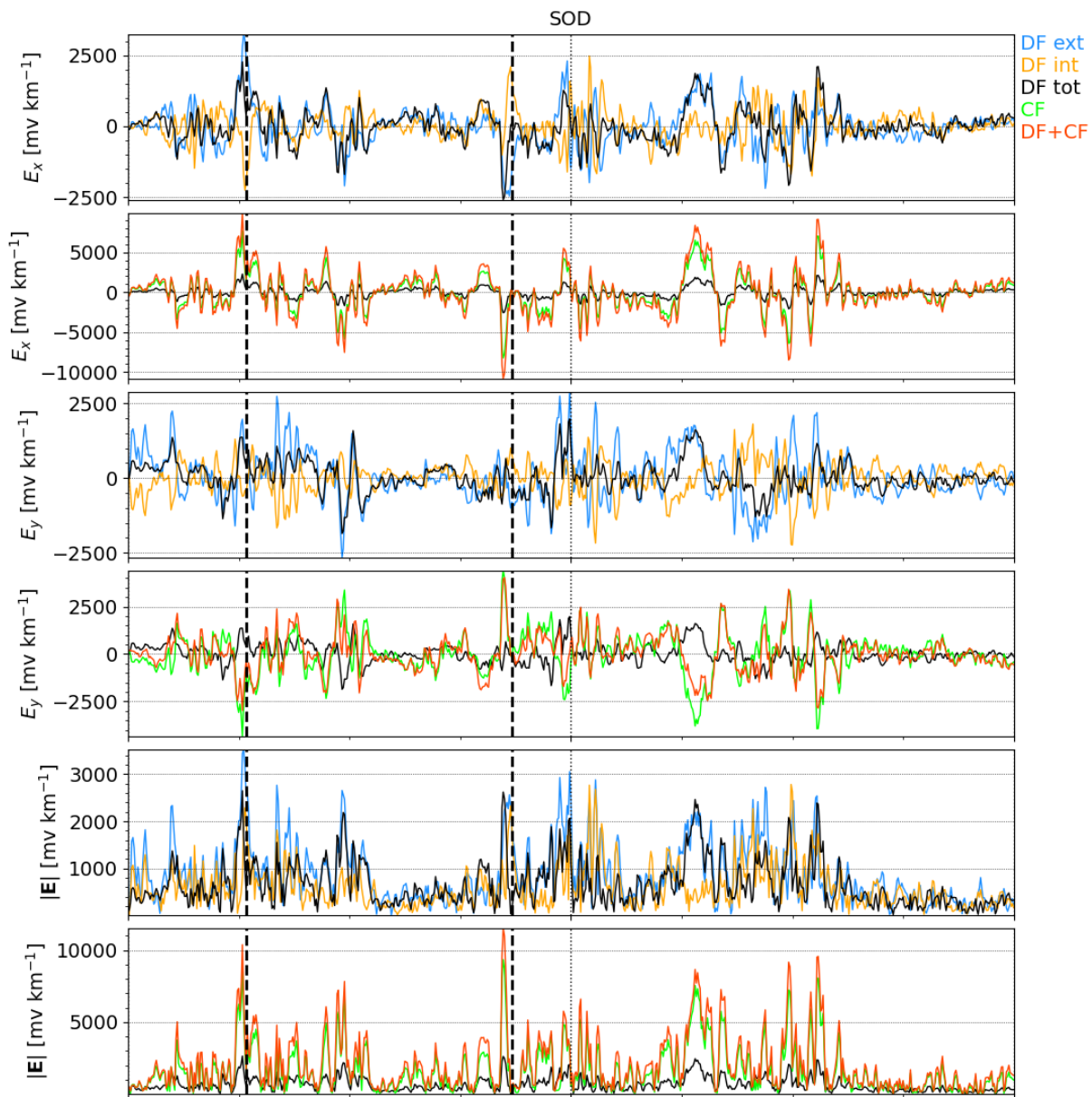




Figure 15. Time series of the north (x) and east (y) components and amplitudes of the external ($\mathbf{E}_{DF,ext}$) and internal ($\mathbf{E}_{DF,int}$) part of the DF electric field, total ($\mathbf{E}_{DF} = \mathbf{E}_{DF,ext} + \mathbf{E}_{DF,int}$) DF electric field, CF electric field (\mathbf{E}_{CF}), and total ($\mathbf{E}_{DF} + \mathbf{E}_{CF}$) electric field at the location of the magnetometer station SOD between 7 September 2017 23:00 UT and 8 September 2017 01:00 UT. The vertical dashed lines indicate the epochs 23:16 UT and 23:52 UT displayed in Fig. 3, Fig. 4, and Fig. 6.

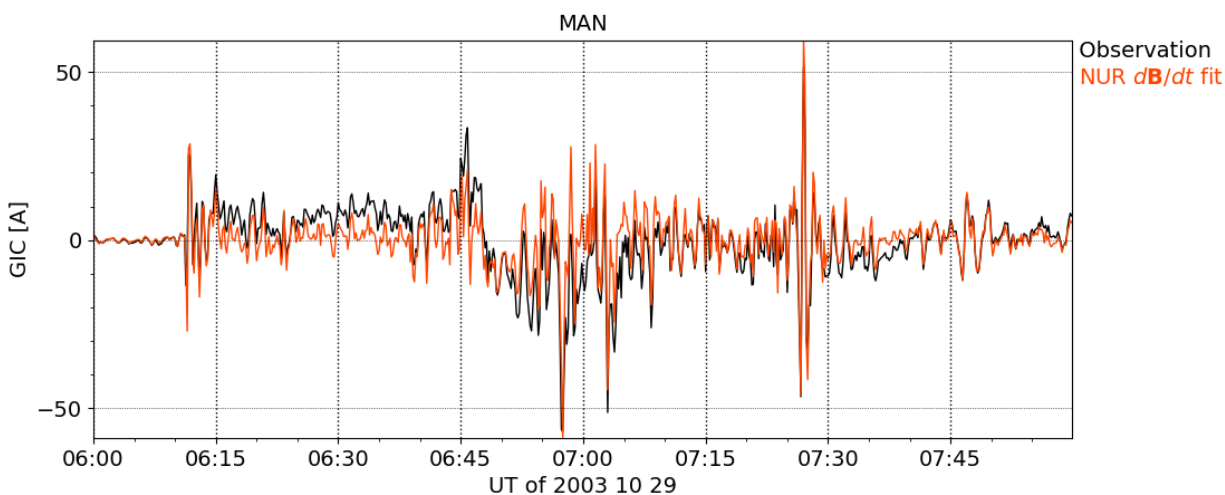


Figure 16. GIC observed at MAN on 29 Oct 2003 from 06:00:00 UT to 07:59:50 UT (black) and GIC modelled based on NUR magnetic field observations using Eq. 37 and the coefficients provided in Table 1.

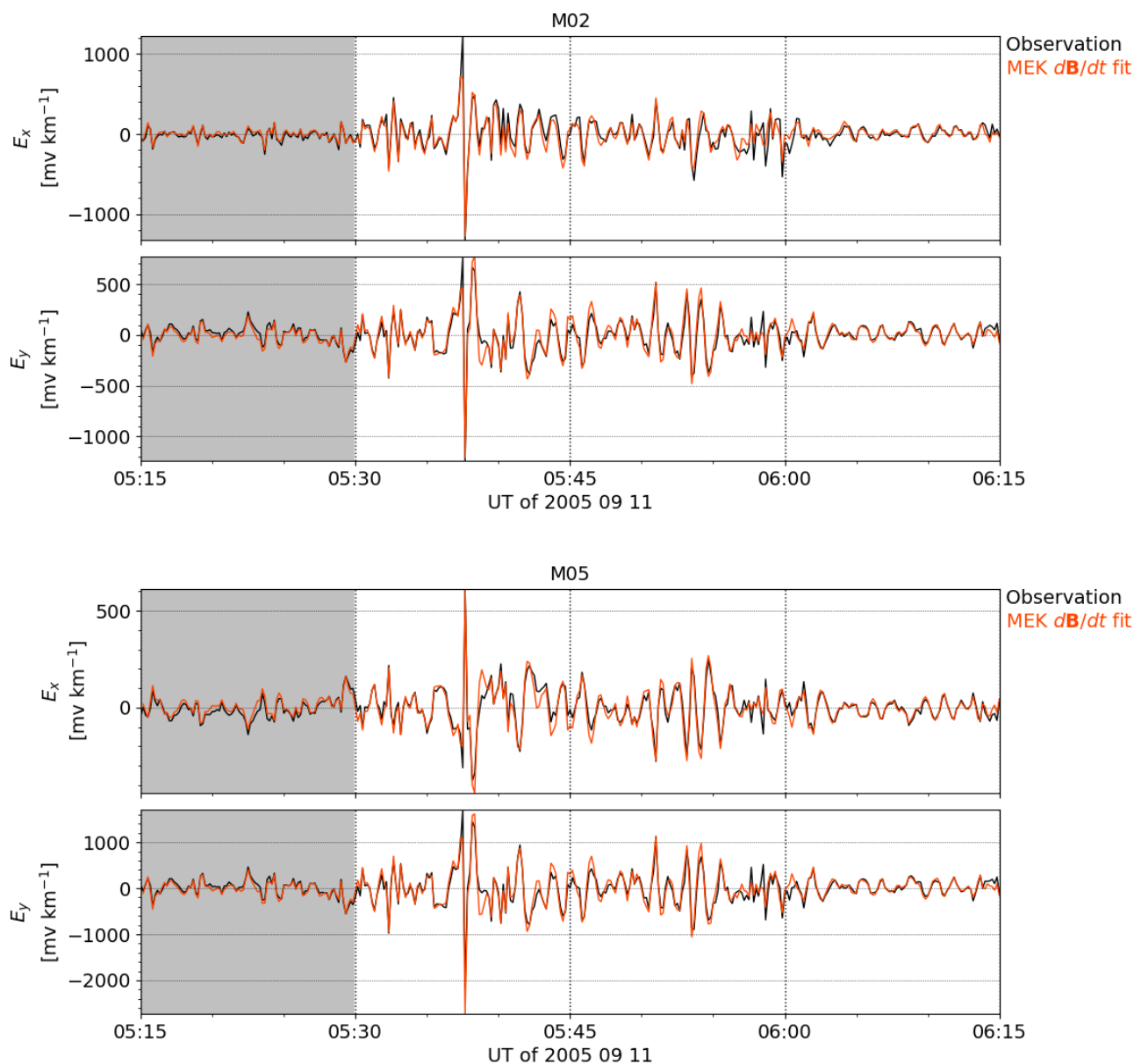


Figure 17. Geomagnetic north (E_x) and east (E_y) components of the geoelectric field observed at the sites M02 (63.043740 N, 30.657030 E) and M05 (62.938890 N, 30.993910 E) on 11 September 2005 from 05:15:00 to 06:15:00 UT (black) and E_x and E_y modelled based on nearby MEK (62.77 N, 30.97 E) geographic magnetic field observations using Eq. 39–40 and the coefficients provided in Table 2. The interval used to determine the coefficients is shaded.

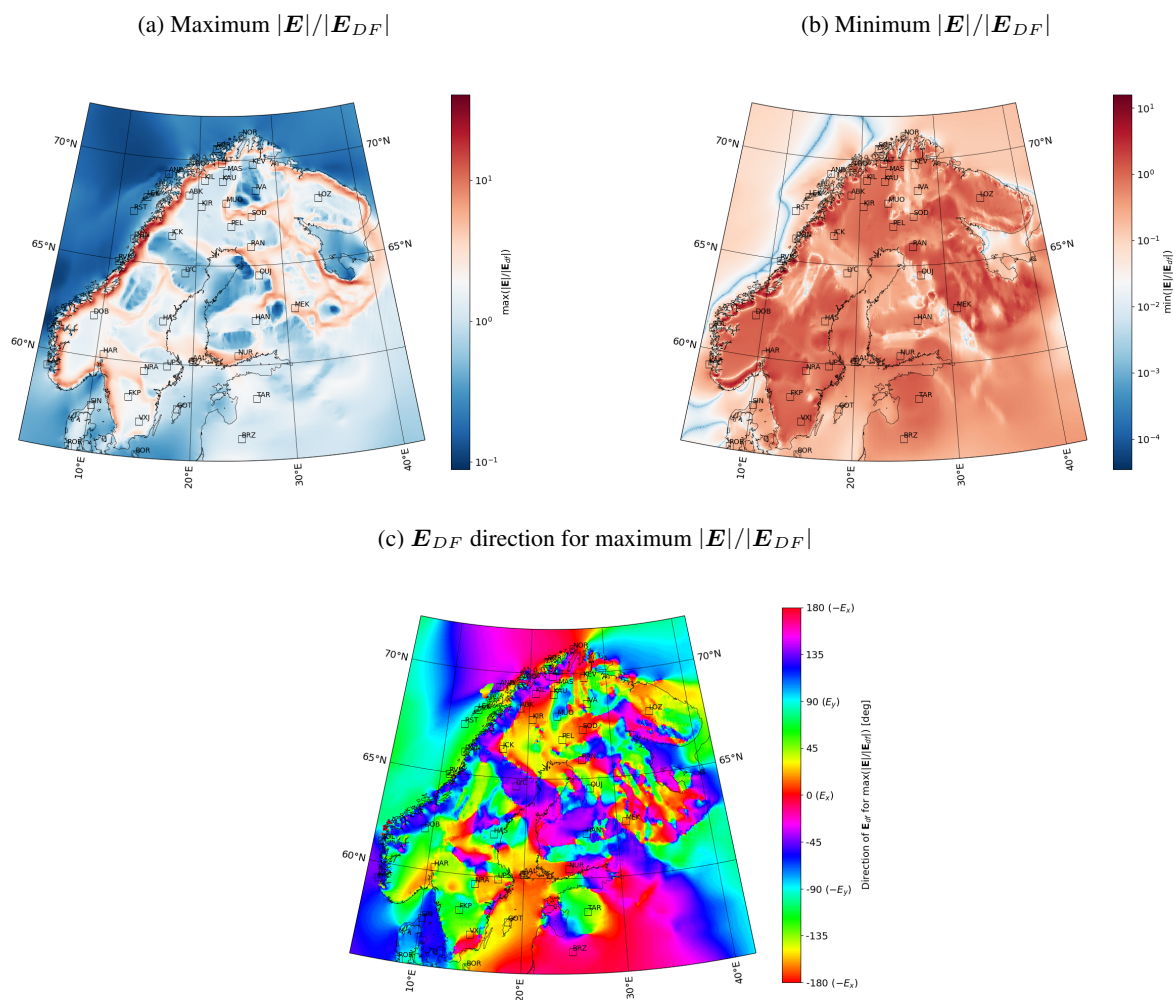


Figure 18. Maximum (top left) and minimum $|\mathbf{E}|/|\mathbf{E}_{DF}|$ (top right), and DF electric field direction where maximum $|\mathbf{E}|/|\mathbf{E}_{DF}|$ is reached (bottom).

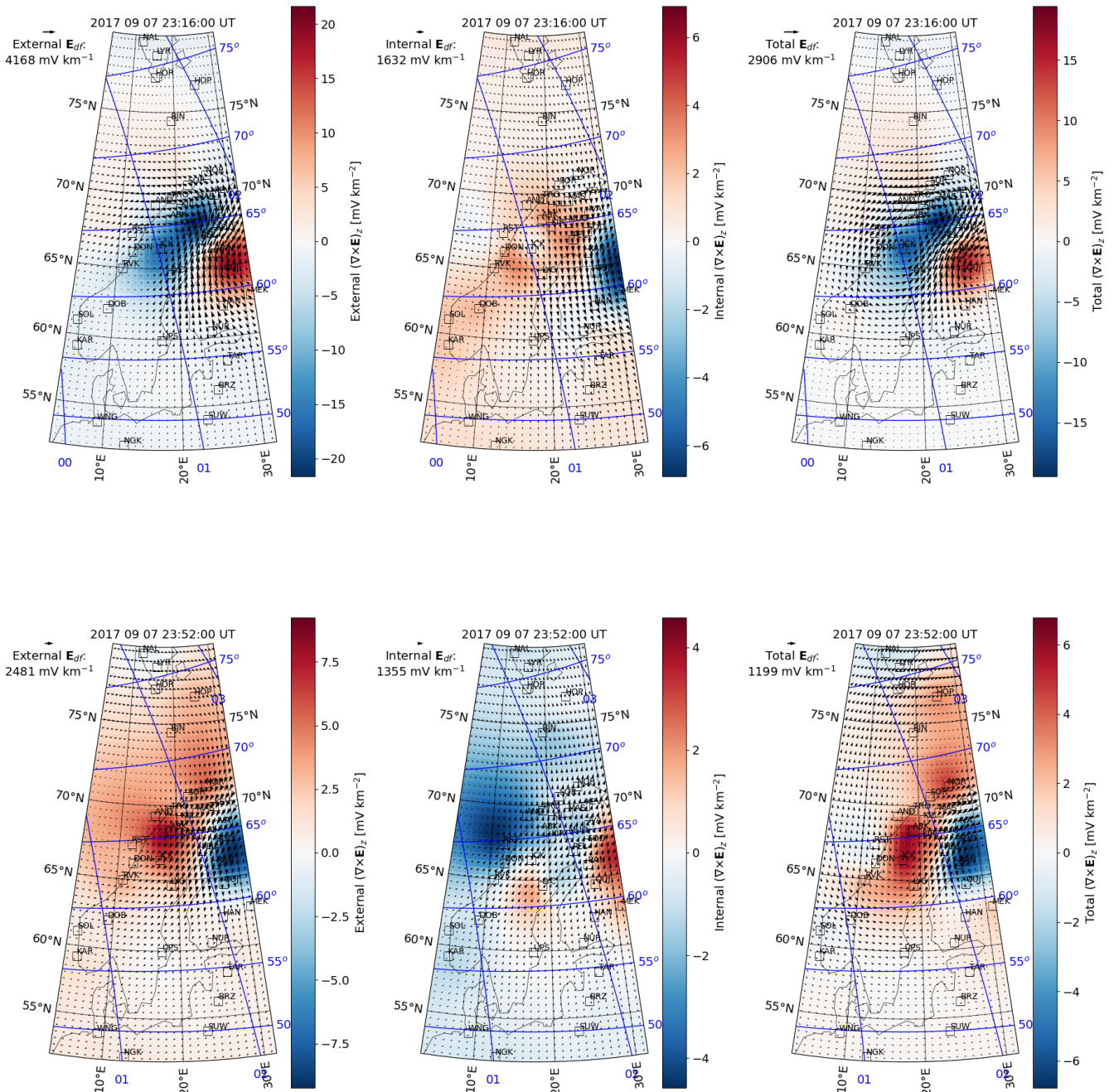


Figure 19. External (left), internal (middle), and total (right) DF electric field (arrows) and its curl (color) in the ionosphere at 90 km altitude on 7 September 2017 at 23:16:00 UT (top) and at 23:52:00 UT (bottom).